The first X-ray look at SMSS J114447.77-430859.3: the most luminous quasar in the last 9 Gyr

E.S Kammoun, Z Igo, J.M Miller, A.C Fabian, M.T Reynolds, A Merloni, D Barret, E Nardini, P.-O Petrucci, E Piconcelli, et al.

Monthly Notices of the ROYAL ASTRONOMICAL SOCIETY

MNRAS **522,** 5217–5237 (2023)
Advance Access publication 2023 April 3

https://doi.org/10.1093/mnras/stad952

The first X-ray look at SMSS J114447.77-430859.3: the most luminous quasar in the last 9 Gyr

E. S. Kammoun [1,2★] Z. Igo [3] J. M. Miller,[4] A. C. Fabian [5] M. T. Reynolds,[4,6] A. Merloni,[3] D. Barret,[1] E. Nardini [2] P. O. Petrucci,[7] E. Piconcelli,[8] S. Barnier,[7] J. Buchner,[3] T. Dwelly [3] I. Grotova,[3] M. Krumpe,[9] T. Liu,[3] K. Nandra,[3] A. Rau,[3] M. Salvato [3] T. Urrutia[9] and J. Wolf[3]

[1]*IRAP, Université de Toulouse, CNRS, UPS, CNES, 9, Avenue du Colonel Roche, BP 44346, F-31028, Toulouse Cedex 4, France*
[2]*INAF – Osservatorio Astrofisico di Arcetri, Largo Enrico Fermi 5, I-50125 Firenze, Italy*
[3]*Max-Planck-Institut für Extraterrestrische Physik (MPE), Giessenbachstrasse 1, D-85748 Garching bei München, Germany*
[4]*Department of Astronomy, The University of Michigan, 1085 S. University Ave., Ann Arbor, MI 48109, USA*
[5]*Institute of Astronomy, University of Cambridge, Madingley Road, Cambridge CB3 OHA, UK*
[6]*Department of Astronomy, The Ohio State University, 140 West 18th Avenue, Columbus, OH, 43210, USA*
[7]*Univ. Grenoble Alpes, CNRS, IPAG, F-38000 Grenoble, France*
[8]*INAF, Osservatorio Astronomico di Roma, Via Frascati 33, I-00078 Monte Porzio Catone, Italy*
[9]*Leibniz-Institut für Astrophysik, Potsdam (AIP), An der Sternwarte 16, D-14482 Potsdam, Germany*

Accepted 2023 March 27. Received 2023 March 15; in original form 2023 February 1

ABSTRACT

SMSS J114447.77-430859.3 ($z = 0.83$) has been identified in the SkyMapper Southern Survey as the most luminous quasar in the last ~ 9 Gyr . In this paper, we report on the eROSITA/*Spectrum–Roentgen–Gamma* (SRG) observations of the source from the eROSITA All Sky Survey, along with presenting results from recent monitoring performed using *Swift*, *XMM-Newton*, and *NuSTAR*. The source shows a clear variability by factors of $\sim$10 and $\sim$2.7 over time-scales of a year and of a few days, respectively. When fit with an absorbed power law plus high-energy cutoff, the X-ray spectra reveal a $\Gamma = 2.2 \pm 0.2$ and $E_{\rm cut} = 23^{+26}_{-5}$ keV . Assuming Comptonization, we estimate a coronal optical depth and electron temperature of $\tau = 2.5 - 5.3\,(5.2 - 8)$ and $kT = 8 - 18\,(7.5 - 14)$ keV , respectively, for a slab (spherical) geometry. The broadband SED is successfully modelled by assuming either a standard accretion disc illuminated by a central X-ray source, or a thin disc with a slim disc emissivity profile. The former model results in a black hole mass estimate of the order of $10^{10}\,{\rm M}_{\odot}$, slightly higher than prior optical estimates; meanwhile, the latter model suggests a lower mass. Both models suggest sub-Eddington accretion when assuming a spinning black hole, and a compact ($\sim 10\,r_{\rm g}$) X-ray corona. The measured intrinsic column density and the Eddington ratio strongly suggest the presence of an outflow driven by radiation pressure. This is also supported by variation of absorption by an order of magnitude over the period of $\sim$ 900 d .

Key words: accretion, accretion discs – galaxies: nuclei – quasars: general – quasars: individual: SMSS J114447.77-430859.3 – quasars: supermassive black holes – X-rays: general.

1 INTRODUCTION

Active galactic nuclei (AGN) are thought to be powered by the accretion of matter onto a supermassive black hole (SMBH) in the form of a disc. The primary hard X-ray continuum in AGN arises from repeated Compton up-scattering of UV/soft X-ray accretion disc photons in a hot, trans-relativistic plasma. This process typically results in a power-law spectrum extending to energies determined by the electron temperature in the hot corona (e.g. Lightman & White 1988; Haardt & Maraschi 1993). Broad-band UV/X-ray spectra require that the corona does not fully cover the disc (Haardt, Maraschi & Ghisellini 1994). X-ray microlensing experiments are suggestive of a compact corona in some bright quasars (QSOs) with a half-light radius smaller than $\sim 6\,r_{\rm g}$ (e.g. Chartas et al. 2009; Mosquera et al. 2013), where $r_{\rm g} = GM_{\rm BH}/c^2$ is the gravitational radius. Eclipses of the X-ray source have also placed constraints on the size of the hard X-ray emitting region(s): $r \leq 10^{14}$ cm (e.g. Risaliti et al. 2007). In addition, spectral-timing studies of X-ray reflection in AGN are also suggestive of a centrally located, compact corona (e.g. Kara et al. 2016; Marinucci et al. 2016).

Most of our detailed knowledge of AGN, and in particular of their X-ray properties, is based on the study of nearby, low-mass, low-accretion rate sources. However, understanding the black hole growth, the energetics of AGN, and the disc-corona connection (among other properties) would require deep observations of high-mass and high-accretion rate sources. Accretion theory predicts that at high accretion rates, the standard radiatively efficient, optically thick, and geometrically thin disc (Shakura & Sunyaev 1973) breaks down. In this case, the radiation pressure becomes more important, and the disc becomes both optically and geometrically thick, a configuration known as a slim disc (e.g. Abramowicz et al. 1988). However,

★ E-mail: ekammoun@irap.omp.eu

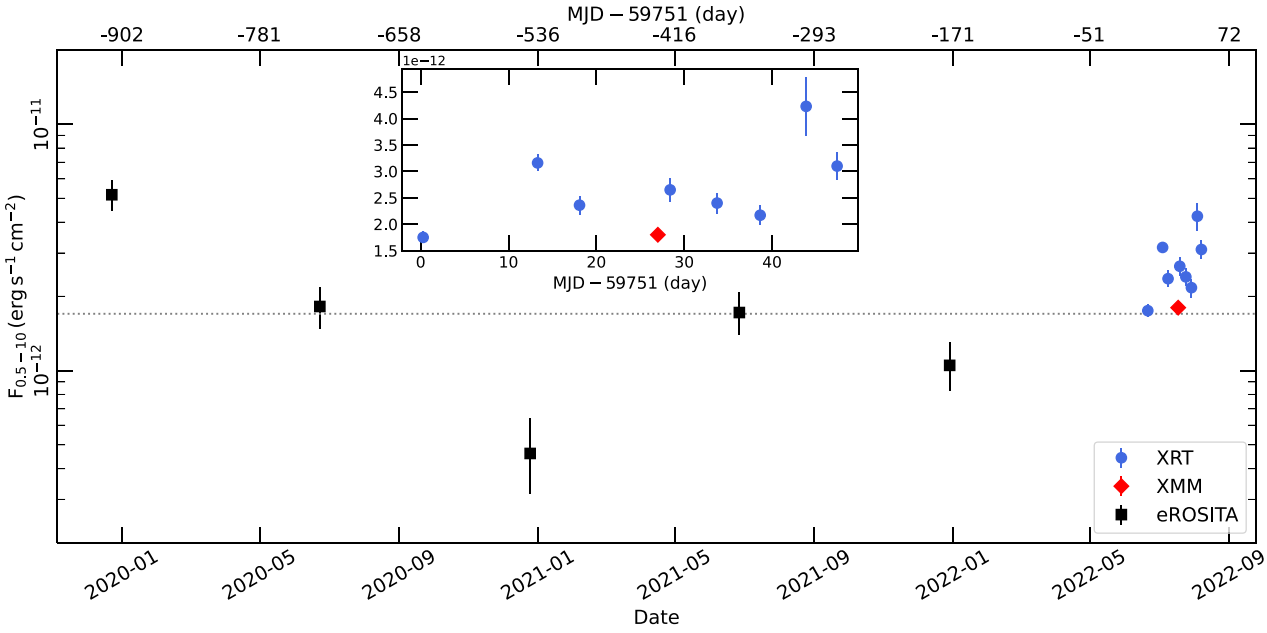

Figure 1. The light curve of J1144 in the 0.5–10 keV band. The black squares, blue circles, and red diamond correspond to eROSITA, *Swift*, and *XMM-Newton*, respectively. The inset shows a zoom-in on the recent monitoring of the source in 2022, with the start being the first *Swift* observation (MJD = 59751). The grey dotted line corresponds to the 3σ upper detection limit by ROSAT obtained in 1990 (see text for details).

recent studies showed that the broadband spectral energy distributions of super- and sub-Eddington AGN do not seem to exhibit any strong differences (e.g. Castelló-Mor et al. 2017; Liu et al. 2021). Whilst high-mass sources are expected to show little or no variability, surprisingly, X-ray observations showed that $\sim 15-25$ per cent of these AGN exhibit large variability (exceeding a factor of 10) in the super-Eddington regime (e.g. Liu et al. 2019, 2021). Moreover, a sizable fraction ($\sim 30-40$ per cent) of high-Eddington quasars seems to be X-ray weak, both at intermediate ($z = 0.5$–1) and high ($z = 2$–4) redshift (e.g. Nardini et al. 2019; Zappacosta et al. 2020; Laurenti et al. 2022). This fraction is much higher than the fraction of X-ray weak sources in non-jetted 'standard' QSOs.

It is worth noting that the studies of such sources have a strong impact on our understanding black hole growth, as well as their impact on their close environment. In fact, the formation of SMBHs with masses of the order of $M_{\rm BH} > 10^9\,{\rm M}_\odot$ at redshifts of $z \sim 6$–7 (i.e. when the Universe was less than 1 Gyr old) is still debated. It has been proposed that one of the channels of forming such massive black holes would be via gas accretion at rates comparable/higher than the Eddington limit (Johnson & Haardt 2016). In addition, these sources are thought to launch powerful nuclear outflows (Nardini et al. 2015; Matzeu et al. 2017), imprinting absorption lines in the X-ray spectra (especially in the 6–8 keV range), that are capable of regulating the growth and the evolution of their host galaxies (e.g. King & Pounds 2015; Giustini & Proga 2019). Thus, highly accreting sources are unique laboratories to study AGN feedback, probing the real impact of nuclear activity on the evolution of massive galaxies and on the formation of structures in the Universe.

SMSS J114447.77-430859.3

Onken et al. (2022) reported on the discovery of SMSS J114447.77-430859.3 ($z = 0.83$; hereafter, J1144) in the SkyMapper Southern Survey (SMSS; Wolf et al. 2018; Onken et al. 2019), as the most luminous quasar of the last ∼9 Gyr observed so far. Using broad hydrogen and magnesium emission lines, the authors estimated a black hole mass of $\log(M_{\rm BH}/{\rm M}_\odot) = 9.4 \pm 0.5$. They also estimated the bolometric luminosity to be $L_{\rm bol} = (4.7 \pm 1.0) \times 10^{47}\,{\rm erg\,s^{-1}}$, suggesting an Eddington ratio of $\lambda_{\rm Edd} = L_{\rm bol}/L_{\rm Edd} \simeq 1.5^{+3.3}_{-1.1}$. This source was not detected in the ROSAT All Sky Survey (RASS). However, interestingly, the examination of five single passes of the eROSITA All-Sky Survey (eRASS1–5), which are each around four times deeper than RASS, confirmed not only the detection of this source, but also a large variability over the course of 2 yr as seen in Fig. 1. In this paper, we present the eRASS1–5 observations of this source. We also present the results obtained from our recent monitoring of the source using the *Neil Gehrels Swift Observatory (Swift)*, *XMM-Newton*, and *NuSTAR*, performed in 2022. J1144 is a unique, closer proxy of luminous QSOs, usually found at cosmic noon ($z \sim 2$–3), that require very deep observations in order to study their X-ray/UV/optical properties.

The paper is structured as follows: the data reduction is presented in Section 2. Section 3 shows the results obtained by analysing the X-ray spectra. The broadband SED is presented in Section 4. Finally, we discuss our results in Section 5.

2 OBSERVATIONS AND DATA REDUCTION

2.1 eROSITA observations

The extended ROentgen Survey with an Imaging Telescope Array (eROSITA; Predehl et al. 2021), the soft X-ray instrument on board the *Spektrum-Roentgen-Gamma (SRG)* orbital observatory, observed J1144 over a period of 2 yr as it performed its first five eRASS passes (eRASS1–5). The eRASS Ecliptic scanning strategy means that an object at intermediate Ecliptic latitudes (like J1144) passes in the eROSITA field of view around 8–10 times every 6 months, with those passes (each less than 40s) all occurring within 1–2 d.

Data were reduced in the standard way using the eROSITA Science Analysis Software System (eSASS) eSASSusers_211214 pipeline version c020 and c947 for eRASS1–4 and 5, respectively (Brunner et al. 2022, Merloni et al., in preparation). A simple astrometric match was used to identify the eROSITA-detected source, as this is robust for high count rate sources with sub-arcsecond positional uncertainties. Exposure corrected spectral extraction of a circular source and annular background region was carried out using `srctool` as described in section 2.2 of Liu et al. (2022). The source extraction radius was defined in a way to maximize the signal to noise and increases in size with the flux of the source, whilst the inner radius of the background annulus is chosen such that the surface brightness of the source's PSF wings is < 2 per cent of the local background surface brightness; both regions mask out other contaminating sources (Brunner et al. 2022; Liu et al. 2022). Subsequently, spectral fitting was done using the `pyXspec` X-ray analysis environment of XSPEC v12.12.0 (Arnaud 1996; Gordon & Arnaud 2021) coupled with Bayesian X-ray Analysis (`BXA v4.0.0`; Buchner et al. 2014, 2021b), a Bayesian parameter estimation and model comparison software using the nested sampling algorithm UltraNest (Buchner 2021a). The spectra, grouped by each single-pass eRASS, from the source and background regions were jointly fitted using a source model, typically an absorbed power law, plus background model. The background model was calculated following Simmonds et al. (2018), by applying Principal Component Analysis (PCA) on an existing parametric model for eROSITA background spectra and adding Gaussian lines until it no longer improved the fit, as judged by the Akaike Information Criterion (see also section 3.1 of Liu et al. 2022 for more details). The shape of this component was therefore already fixed in the joint modelling, however, the normalization was left free to vary so it could adjust to the required background flux level.

Light curves were also extracted using eSASS and analysed using `bexvar` to search for variability (Buchner et al. 2022). Variability in `bexvar` is quantified by the intrinsic scatter ($\sigma_{\rm bexvar}$) on the assumed log-normal distribution of count rates in any given time bin (see section 3 of Buchner et al. 2022). This log-scatter on the log-count rate is similar in concept to the excess variance on the linear count rate, usually quoted as the normalized excess variance (NEV; e.g. Vaughan et al. 2003).

2.2 *Swift* observations

Swift observed J1144 in 10 occasions over a period of 47 d, from 2022-06-21 to 2022-08-07 (Obsid 15227001–15227010, hereafter XRT/O1–O10, respectively). Two of these observations (O2 and O5) were too short, resulting in less than 20 counts in total, thus we omitted them from this analysis. The X-ray telescope (XRT; Burrows et al. 2005) operated during these observations in the Photon Counting (PC) mode. We reduced the data following standard procedures using `HEASOFT` [Nasa High Energy Astrophysics Science Archive Research Center (Heasarc) 2014]. We performed the initial reduction with `xrtpipeline`. Source and background spectra were extracted using `xselect` from circular regions of 50 arcsec in radius. We used the default redistribution matrix file and ancillary response file, available in the calibration database. The spectra were then binned, requiring a minimum signal-to-noise ratio (S/N) of 3 per energy bin.

J1144 was simultaneously observed in the optical/UV by the *Swift*/UVOT (Roming et al. 2005). All observations were analyzed in the `HEASOFT-6.30.1` environment utilizing the latest version of the UVOT CALDB. All image segments contained in a given obsid are summed prior to source detection. The flux from J1144 was calculated using the `uvotmaghist` task with a 5 arcsec source region centred on the known coordinates of J1144. Background was estimated from a nearby source free region. The UVOT light curves are shown in Fig. 2.

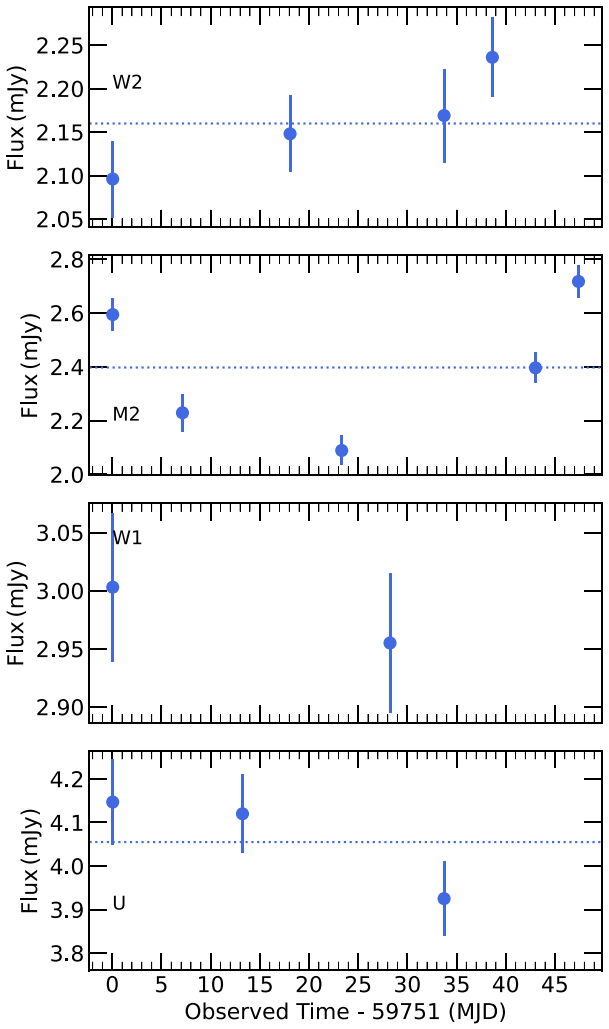

Figure 2. UVOT light curves obtained during the monitoring of the source in 2022. The horizontal dotted lines represent the average flux in the bands with more than two data points.

2.3 *XMM-Newton* observation

XMM-Newton observed J1144 on 2022-07-18 (ObsID 0911791701) for a total exposure of 15 ks. The observation was operated in the Full Frame/Thin Filter mode for EPIC-pn (Strüder et al. 2001) and the two EPIC-MOS (Turner et al. 2001) instruments. We reduced the data using SAS v.19.1.1 (Gabriel et al. 2004) and the latest calibration files. We processed the data using `EPPROC` and `EMPROC` for the EPIC-pn and EPIC-MOS, respectively. Source spectra were extracted from a circular region of radius 30 arcsec centred on the source. The corresponding background spectra were extracted from an off-source circular region located on the same CCD chip, with a radius twice that of the source. We filtered out periods with strong background flares estimated to be around 5.5 ks for EPIC-pn and 1.4 ks for EPIC-MOS. Response matrices were produced using the `FTOOLsRMFGEN` and `ARFGEN`. We rebinned the observed spectra

Table 1. Log of the X-ray observations.

Date (MJD)	Instrument	Net count rate (Count s^{-1})	Net exp. (ks)
58840	eROSITA/eRASS1	3.7 ± 0.3	0.15
59023	eROSITA/eRASS2	1.5 ± 0.3	0.10
59208	eROSITA/eRASS3	0.4 ± 0.2	0.10
59392	eROSITA/eRASS4	1.2 ± 0.3	0.11
59577	eROSITA/eRASS5	1.0 ± 0.3	0.12
59751	XRT/O1	0.039 ± 0.003	3.6
59764	XRT/O3	0.059 ± 0.005	2.2
59769	XRT/O4	0.041 ± 0.005	1.7
59779	XRT/O6	0.042 ± 0.005	1.4
59785	XRT/O7	0.036 ± 0.005	1.7
59790	XRT/O8	0.037 ± 0.004	1.6
59795	XRT/O9	0.056 ± 0.008	0.7
59798	XRT/O10	0.058 ± 0.007	1.2
59778	*XMM-Newton*/PN	0.538 ± 0.007	9.7
	XMM-Newton/MOS2	0.158 ± 0.003	13.7
59759	*NuSTAR*/FPMA	0.024 ± 0.0006	61.6
	NuSTAR/FPMB	0.022 ± 0.0007	60.9

The net count rates are reported in the 0.2–5 keV range for eROSITA, the 0.4–5 keV for XRT, 0.4–10 keV for *XMM-Newton*, and 3.5–30 keV for *NuSTAR*.

using the SAS task SPECGROUP to have a minimum S/N of 4 in each energy bin. The EPIC-MOS1 observation suffered from a bad column coincident with the location of the source. Thus, we use in the following analysis the results from EPIC-pn and EPIC-MOS2 only.

2.4 *NuSTAR* observation

J1144 was observed by *NuSTAR* on 2022-06-28 (ObsID 90801616002) for a total exposure of 130 ks (net exposure of ∼61 ks). The data were reduced using the standard pipeline in the *NuSTAR* Data Analysis Software (NUSTARDAS v2.0.0), and using the latest calibration files. We cleaned the unfiltered event files with the standard depth correction. We reprocessed the data using the $saamode = optimized$ and $tentacle = yes$ criteria for a more conservative treatment of the high background levels in the proximity of the South Atlantic Anomaly. We extracted the source and background light curves and spectra from circular regions of radii 50 arcsec, for the two focal plane modules (FPMA and FPMB) using the HEASOFT task nuproducts. We binned the spectra to require a minimum S/N of 4 in each energy bin. The *NuSTAR* light curves do not show any signature of variability during the observation. In the following we analyse the spectra from FPMA and FPMB jointly, without combining them together.

The details of each of the observations are shown in Table 1. Fig. 1 shows the observed flux in the 0.5–10 keV light curves for eROSITA, *Swift*, and *XMM-Newton* (black squares, blue circles, and red diamond, respectively). The fluxes are estimated based on the best-fitting models (see next section for details). We used the HIgh-energy LIght curve GeneraTor[1] (HILIGT; Saxton et al. 2022) to derive an upper limit on the ROSAT non-detection. This gives a 3σ upper limit on the $0.2-2$ keV flux of 1.4×10^{-12} erg s^{-1} cm^{-2}. Assuming $\Gamma=2$, this translates into a $0.5-10$ keV flux upper limit of 1.7×10^{-12} erg s^{-1} cm^{-2}. This is consistent with the flux values during eRASS2–5 and the early observations of the 2022 monitoring.

[1] http://xmmuls.esac.esa.int/hiligt/

Table 2. UVOT light curve of the source obtained in the different filters.

Date (MJD)	Filter	Flux (mJy)
59751	W2	2.10 ± 0.04
59751	M2	2.59 ± 0.06
59751	W1	3.00 ± 0.06
59751	U	4.15 ± 0.10
59751	B	4.90 ± 0.10
59751	V	6.24 ± 0.16
59758	M2	2.23 ± 0.07
59764	U	4.12 ± 0.09
59769	W2	2.15 ± 0.04
59774	M2	2.09 ± 0.05
59779	W1	2.96 ± 0.06
59785	U	3.93 ± 0.09
59785	W2	2.17 ± 0.05
59790	W2	2.24 ± 0.05
59794	M2	2.40 ± 0.06
59798	M2	2.72 ± 0.06

3 X-RAY SPECTRAL ANALYSIS

3.1 eRASS results

As mentioned before, we use bexvar to assess whether any significant temporal variability exists within any given eRASS, by looking at the log-scatter on the log-count rate. For J1144, this typical 'intra-eRASS' variability time-scale is around 4 h. However, low values of $\sigma_{\rm bexvar} \ll 0.1$ are consistently found for all eRASS1–5 over several energy bands. Overall, the long term (inter-eRASS) X-ray variability, clearly seen in Fig. 1, is much more significant than the short term (intra-eRASS) variability. For that reason, in the following, we model the time-averaged spectrum from each eRASS.

We model the spectra using a simple absorbed power law ($TBabs \times zTBabs \times zpow$ in XSPEC formalism), where TBabs and zTBabs (Wilms, Allen & McCray 2000) correspond to the Galactic absorption in the line of sight and the intrinsic neutral absorption at the redshift of the source, respectively. We fixed the Galactic column density at $N_{\rm H}=7.9\times10^{20}$ cm^{-2} (HI4PI Collaboration 2016) but the intrinsic column density ('znH1–5'), the power law photon index ('PhoIndex1-5'), and power-law normalizations ('norm1-5') were left free for each eRASS spectrum. Upon modelling each spectrum individually, it is found that the intrinsic column density and photon index are consistent with each other across eRASS1–5, albeit with large uncertainties, due to the quality of the data. Yet, the values of the normalizations were showing a clear variability across the five spectra. For this reason, we re-fit the spectra simultaneously by tying the column density and the photon index for all observations, and keeping the normalization free to vary. The prior set on the column density, the photon index, and the normalizations was a log-uniform prior ranging from $(10^{-3}-10^{3})\times10^{22}$ cm^{-2}, a uniform prior from 1 to 4, and a log-uniform prior from 10^{-6} to 10 photon keV^{-1} cm^{-2} s^{-1}, respectively.

Fig. 3 showcases the results of this simultaneous fitting of eRASS1–5 spectra. The top panel shows the deconvolved spectra, to better compare with observations from different instruments. The middle panel shows the convolved spectra, folded through detector response but not effective area, along with background spectra (dotted lines). It is clear that the background becomes dominant past $2-3$ keV. The normalized residuals are also displayed in the bottom panel of the same figure. The apparent difference in the levels of background are caused by the varying extraction region

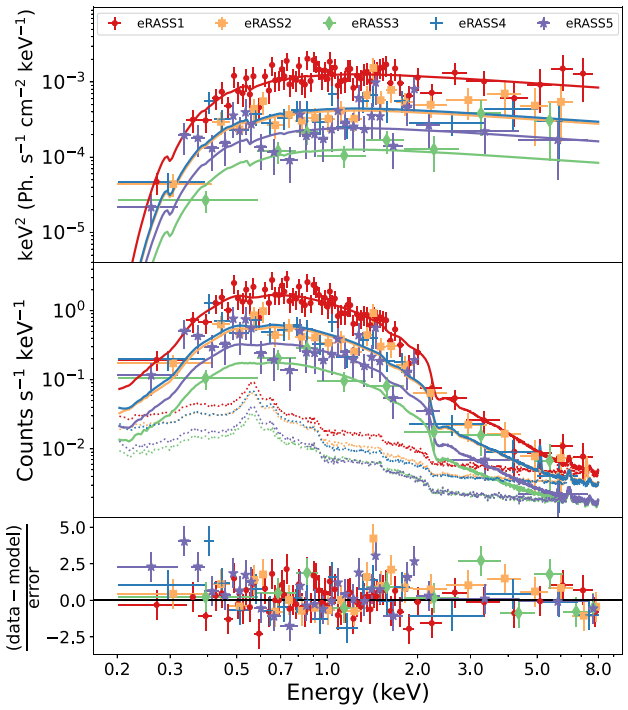

Figure 3. Observed spectra from the different eROSITA observations (eRASS1 − 5: red circle, yellow square, green diamond, blue cross, purple star). Top: Deconvolved spectra. Middle: Convolved spectra, folded through detector response but not effective area, along with background spectra for each eRASS (dotted, same colour scheme). Bottom: Normalized residuals obtained by fitting the spectra.

sizes, which scale proportional to the source flux. Quantitatively, the eRASS1 (highest flux state) source extraction region area is a factor of ∼3 larger than that of eRASS3 (lowest flux state), and this is reflected in the difference in normalization between the red and green dotted lines. The best-fitting (posterior median) photon index and 3σ upper limit on the column density for eRASS1–5 are $\Gamma = 2.21^{+0.14}_{-0.12}$ and $N_{\rm H} < 2.7 \times 10^{21}$ cm^{-2}, respectively. Moreover, we find a factor >10 decrease in the normalization of the power law between eRASS1 and eRASS3, after which it steadily increases again up till eRASS5. Table 3 lists the best-fitting parameters for this simultaneous fitting of eRASS1–5 spectra. The corner plot in Fig. C1 shows the parameter space sampled during the fit procedure and the posterior distributions obtained for each parameter (znH, PhoIndex, norm1–5). The confidence contours are drawn at 68th and 95th percentiles. Note that BXA methodology is fully consistent with the Levenberg–Marquardt minimization algorithm used in XSPEC, however, BXA is preferred for modelling eROSITA sources as the sampling remains unbiased even in the low count regimes.

3.2 2022 monitoring

In the rest of the spectral analysis we use XSPEC V12.11.1 (Arnaud 1996). We fit simultaneously the data from all of the *Swift*/XRT, *XMM-Newton*, and *NuSTAR* data assuming the following model:

$$\texttt{Model} = \texttt{TBabs} \times \texttt{TBpcf} \times \texttt{cflux} \times \texttt{zcutoffpl}, \quad (1)$$

where `TBabs` corresponds to the Galactic absorption in the line of sight of the source. `TBpcf` corresponds to a partially covering neutral absorption at the rest frame of the source. The `cflux` component measures the flux of the power-law component with a high-energy cutoff (`zcutoffpl`) in the 2–10 keV range. We kept the column density of the `TBpcf` component constant for all observations, but we let the covering fraction ($f_{\rm cov}$) free to vary. We also kept the photon index (Γ) and the high-energy cutoff ($E_{\rm cut}$) constant for all observations and we let the flux free. The spectra together with the best-fitted model are shown in Fig. 4. The corresponding residuals are shown in Fig. B1. All uncertainties are listed with 1σ confidence level. We present in Appendix A the results obtained by performing a line search on the *XMM-Newton* spectra. This results in hints of an absorption line at ∼ 1.3 keV, and an emission line at ∼ 6.5 keV, with a significance of $\sim 3\sigma$.

The model is statistically accepted with $\chi^2/{\rm dof} = 346.7/320$ ($p_{\rm null} = 0.15$). We obtained a best-fitting $\Gamma = 2.0 \pm 0.1$, $E_{\rm cut} = 68^{+65}_{-23}$ keV, and $N_{\rm H} = (3.7 \pm 0.6) \times 10^{22}$ cm^{-2}. The best-fitting results show hints of variability in $f_{\rm cov}$ that cannot be strongly constrained due to the quality of the data. However, the changes in the 2–10 keV flux can be clearly confirmed with a max-to-min ratio of ∼2.7 over the period of the monitoring (see Fig. 5). The best-fitting photon index obtained from this monitoring of the source is consistent within uncertainties with the one obtained by modeling the eROSITA spectra.

For completeness, we tested a model by replacing `TBpcf` in equation (1) by a warm absorption model, `zxipcf`. We kept the column density and the covering fraction constant for all observations and let the ionization parameter vary. This resulted in a worse fit than using the neutral absorption ($\chi^2/{\rm dof} = 357/320$). Keeping the ionization parameter constant and letting the covering fraction free to vary results in a comparable fit to the one with `TBpcf`, with an ionization parameter consistent with a neutral absorption, deriving an upper limit of $\log \xi < 1.5$.

4 BROADBAND SPECTRAL ENERGY DISTRIBUTION

4.1 KYNSED

First, we use `KYNSED`[2] (Dovčiak et al. 2022) to model the broadband SED of the source. This model considers a Novikov–Thorne (Novikov & Thorne 1973) accretion disc that powers the X-ray corona, assumed to be a point source located on the rotational axis of the SMBH. The fraction of the power transferred from the accretion disc to the corona is denoted by $L_{\rm transf}/L_{\rm disc}$. The X-ray corona emits then a primary power-law continuum which partially arrives to the observer and partially irradiates the disc. The disc will reprocess the incident emission. A part of this emission is re-emitted in the form of an X-ray reflection spectrum, and the other part is absorbed by the disc. This absorbed radiation will heat the disc and will be re-emitted in the UV/optical as an additional thermal emission. This process explained successfully the observed UV/optical continuum time-lags (see e.g. Kammoun, Papadakis & Dovčiak 2019, 2021a) as well as the power spectral density (Panagiotou et al. 2020, 2022), obtained from intense monitoring of local AGN. Dovčiak et al. (2022) used `KYNSED` to model the broadband SED obtained from the long monitoring of NGC 5548. The authors discuss in their section 5.5 the fact that the code does not take variability into account in its computations. Thus, the code is not ideal for modelling simultaneous X-ray/UV/optical observations. Instead, it is more suited for modeling time-averaged SEDs. For that reason, we constructed the time-averaged spectrum

[2] https://projects.asu.cas.cz/dovciak/kynsed

Table 3. Best-fitting parameters obtained by modelling the eROSITA spectra.

$N_{\rm H}[{\rm cm}^{-2}]$	Γ	log(norm1)	log(norm2)	log(norm3)	log(norm4)	log(norm5)
$<2.7\times10^{21}$	$2.21^{+0.14}_{-0.12}$	$-2.27^{+0.06}_{-0.05}$	$-2.72^{+0.07}_{-0.06}$	$-3.31^{+0.09}_{-0.10}$	$-2.75^{+0.06}_{-0.06}$	$-2.97^{+0.08}_{-0.06}$

Note that the intrinsic column density ($N_{\rm H}$) is a 3σ upper limit. Normalizations (norm1–5) are in units of Photon keV^{-1} cm^{-2} s^{-1}.

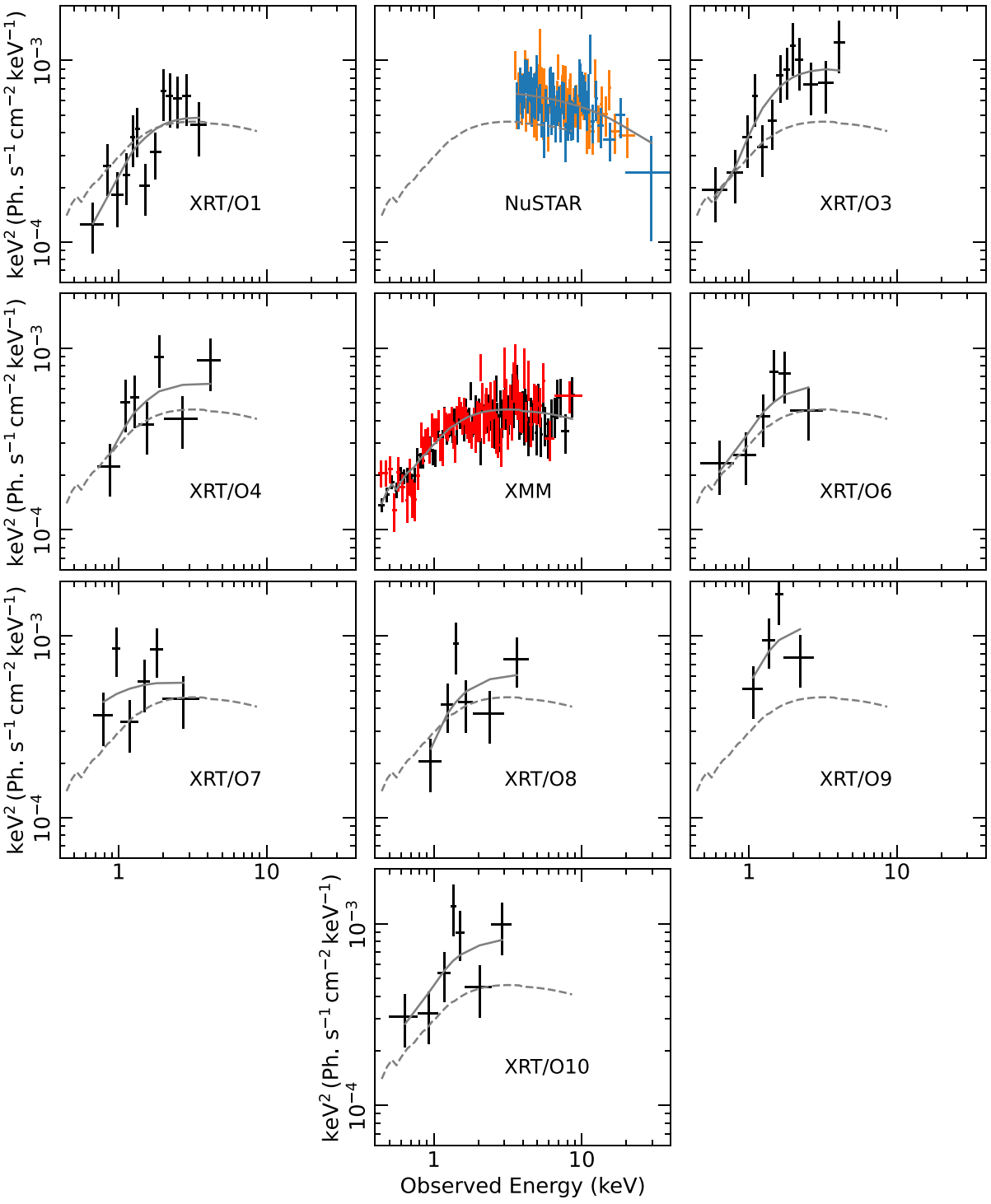

Figure 4. *Swift*, *XMM-Newton*, and *NuSTAR* spectra obtained during the monitoring of J1144 in 2022. The solid lines correspond to the best-fitting model assuming an absorbed power law (see Section 3.2). The dashed lines represent the best-fitting model to the *XMM-Newton* data, for comparison.

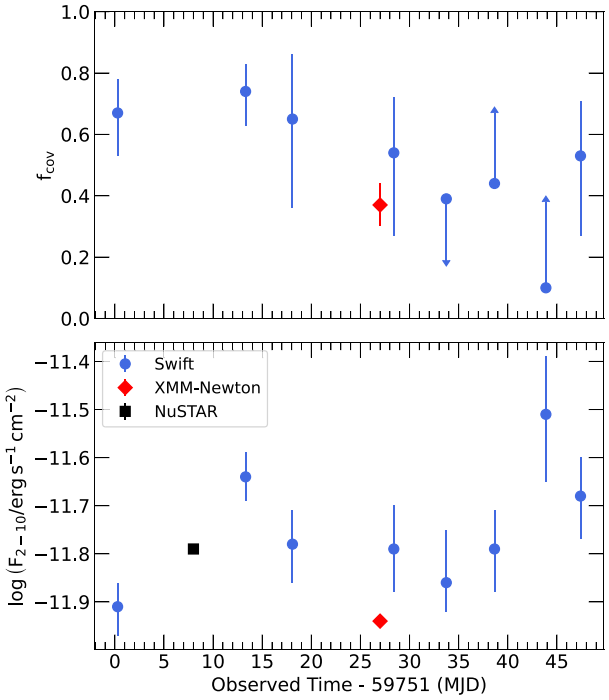

Figure 5. Variability of f_{cov} and the 2–10 keV flux during the monitoring of J1144 in 2022.

from the UVOT monitoring. To do so, we estimated the average flux of the source in bands with three or more observations. These are the UVW2, UVM2, and U bands, only. As for the X-ray spectra, we considered the *XMM-Newton* and *NuSTAR* ones, which, together, should be representative of the average state of J1144.

In XSPEC parlance, the model can be written as follows:

$$\texttt{Model} = \texttt{redden}_{\texttt{UV/opt}} \times \texttt{TBabs}_{\texttt{X}} \times \texttt{TBpcf}_{\texttt{X}} \times \texttt{KYNSED}. \quad (2)$$

All the relevant KYNSED parameters are tied in the UV and optical range with those in the X-ray range. The $TBabs_X$ component accounts for the effects of the Galactic absorption in the X-ray band. We fix its column density to 7.91×10^{20} cm^{-2}. The $redden_{UV/opt}$ component accounts for the reddening due to dust extinction in our Galaxy. We fix the extinction $E(B-V)$ to 0.111 (Schlafly & Finkbeiner 2011). The assumed values of Galactic N_H and $E(B-V)$ are consistent with the observed relation between these two values (e.g. Bohlin, Savage & Drake 1978). $TBpcf_X$ accounts for partially covering absorption in the rest frame of the source. We applied $TBabs_X$ and $TBpcf_X$ to the X-ray spectra only, while $redden_{UV/opt}$ is only applied to the UV/optical data.

The model does not give a statistically acceptable fit when we fix M_{BH} to the value that is reported by Onken et al. (2022). Instead, the fit improves significantly by letting the mass to be larger. Given that many parameters could not be constrained and that some of them are degenerate we adopted the following fitting scheme. We fix the spin to 0, 0.7, and 0.998. For each of the spin values, we choose randomly, assuming a uniform distribution, a combination of coronal height (h), colour correction factor[3] (f_{col}), and inclination (θ). The limits of each parameter are given in Table 5. We fixed the parameters to the chosen values and we fit the SED letting the mass and the accretion rate in units of Eddington[4] ($\dot{m}/\dot{m}_{Edd}$) to be free. In addition, Γ, E_{cut}, N_H, and f_{cov} are left free but tied between the different spectra. We left L_{transf}/L_{disc} untied between *XMM-Newton* and *NuSTAR* ($L_{transf,\,X}/L_{disc}$ ab = nd $L_{transf,\,N}/L_{disc}$, respectively). We repeated this for 500 times for each of the spin values. We selected only the fits that are statistically accepted with (χ^2/dof $< 300/276$, i.e. $p_{null} > 0.15$).

Assuming Comptonization, and using the conservation of photons during this process, KYNSED estimates the size of the corona (R_c) a posteriori (see Dovčiak & Done 2016; Ursini et al. 2020; Dovčiak et al. 2022, for more details). This assumes a spherical source on the rotation axis of the BH. Despite the fact that this computation is approximate, it proved to be aligned with more accurate 3D models (see section 5.3 in Dovčiak et al. 2022). We use this approximation to rule out configurations in which the best-fitting results in a large

[3]This factor corrects for the spectral hardening due to photon interactions with matter in the upper layers of the accretion disc.

[4]The Eddington accretion rate is defined as $\dot{m}_{Edd} = L_{Edd}/\eta c^2$, where η, the radiative efficiency is a function of the BH spin, and $L_{Edd} \simeq 1.26 \times 10^{38} M_{BH}/M_\odot$ erg s^{-1} is the Eddington luminosity.

Table 4. Best-fitting f_{cov} and 2–10 keV flux obtained by fitting the X-ray spectra of the source from the monitoring in 2022.

Observation	f_{cov}	$\log(F_{2-10}/\mathrm{cgs})$
XRT/O1	$0.68^{+0.05}_{-0.13}$	$-11.91^{+0.05}_{-0.06}$
XRT/O3	$0.75^{+0.09}_{-0.11}$	$-11.64^{+0.05}_{-0.05}$
XRT/O4	$0.65^{+0.21}_{-0.29}$	$-11.78^{+0.07}_{-0.08}$
XRT/O6	$0.56^{+0.18}_{-0.27}$	$-11.79^{+0.09}_{-0.09}$
XRT/O7	<0.39	$-11.86^{+0.11}_{-0.06}$
XRT/O8	>0.43	$-11.81^{+0.08}_{-0.09}$
XRT/O9	>0.10	$-11.52^{+0.12}_{-0.14}$
XRT/O10	$0.55^{+0.18}_{-0.26}$	$-11.68^{+0.08}_{-0.09}$
XMM-Newton	$0.44^{+0.07}_{-0.07}$	$-11.93^{+0.01}_{-0.01}$
NuSTAR	–	$-11.79^{+0.01}_{-0.01}$

Table 5. Best-fitting parameters obtained by modelling the SED of J1144 using KYNSED, assuming different values of the spin.

	$a^* = 0$	$a^* = 0.7$	$a^* = 0.998$
$h\,(r_g)$		3–30	
$\theta(^\circ)$		0–60	
f_{col}		1.0–2.4	
$\log M_{BH}/M_\odot$	$10.10^{+0.38}_{-0.47}$	$10.33^{+0.43}_{-0.56}$	$10.55^{+0.62}_{-0.51}$
$\log \dot{m}/\dot{m}_{Edd}$	$0.19^{+0.41}_{-0.28}$	$0.00^{+0.47}_{-0.34}$	$-0.03^{+0.54}_{-0.66}$
Γ	$2.16^{+0.25}_{-0.16}$	$2.17^{+0.27}_{-0.15}$	$2.19^{+0.28}_{-0.19}$
E_{cut} (keV)	23^{+26}_{-5}	22^{+23}_{-6}	22^{+15}_{-7}
$L_{transf,\,X}/L_{disc}$	$0.08^{+0.05}_{-0.04}$	$0.07^{+0.09}_{-0.03}$	$0.05^{+0.07}_{-0.02}$
$L_{transf,\,N}/L_{disc}$	$0.11^{+0.08}_{-0.05}$	$0.10^{+0.15}_{-0.05}$	$0.07^{+0.11}_{-0.03}$
N_H (10^{22} cm^{-2})	$3.39^{+0.46}_{-0.40}$	$3.35^{+0.52}_{-0.32}$	$3.32^{+0.51}_{-0.46}$
f_{cov}	$0.54^{+0.12}_{-0.11}$	$0.55^{+0.13}_{-0.10}$	$0.55^{+0.13}_{-0.12}$
ξ_{in} (erg cm s^{-1})	$0.2^{+2.7}_{-0.2}$	$0.2^{+4.8}_{-0.1}$	$0.5^{+63.5}_{-0.5}$
$R_c\,(r_g)$	$10.1^{+14.5}_{-4.7}$	$6.9^{+19.3}_{-3.8}$	$5.6^{+12.1}_{-3.9}$
$\mathcal{R}$	$0.75^{+0.23}_{-0.25}$	$0.83^{+0.27}_{-0.24}$	$0.89^{+0.68}_{-0.25}$
χ^2	272–294	271–300	271–300
dof		276	

The uncertainties represent the lowest/highest values obtained from the SED modelling (see text for details).

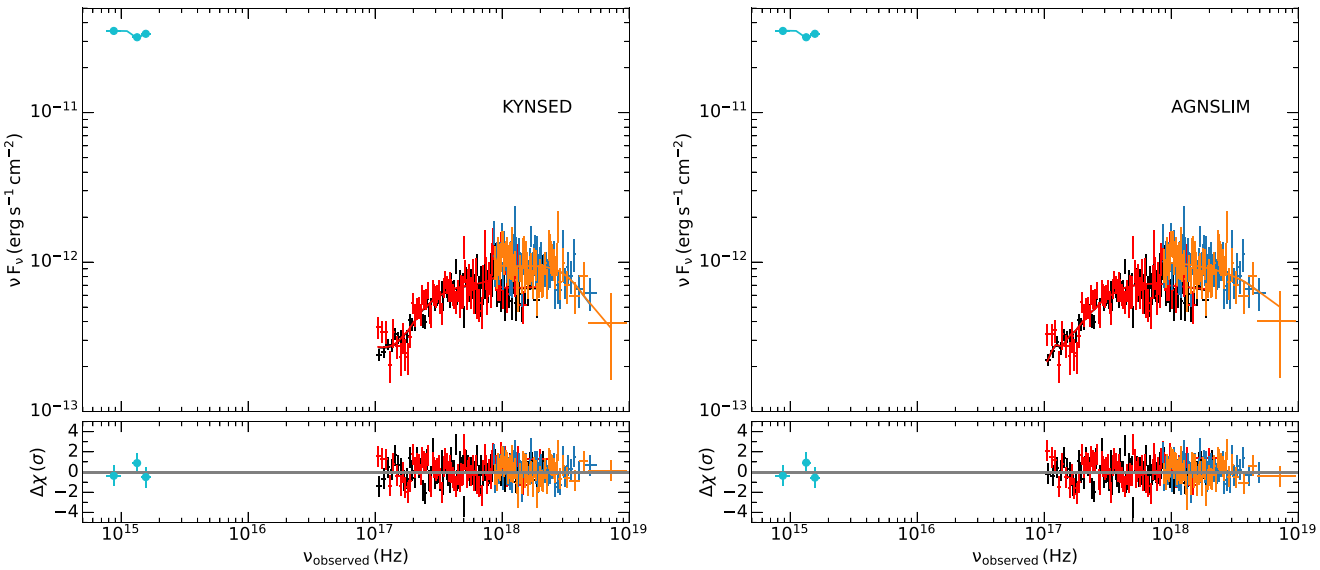

Figure 6. Observed SED of J1144 using *Swift*/UVOT (cyan circles), *XMM-Newton*/pn,MOS (black and red, respectively), and *NuSTAR*/FPMA,FPMB (orange and blue, respectively). The solid line corresponds to one of the best-fitting models obtained for $a^* = 0$ using KYNSED (left) and AGNSLIM (right). The other realizations resulted in a similar quality of the fit (see text for details). The bottom panels show the residuals corresponding to these fits.

corona that is not consistent with the assumptions of the model. This can be used to make an additional selection on the accepted configurations. For that reason, we select from our fits only the results where R_c is smaller than the difference between the height of the source and the event horizon of the BH. This results in a selection of 80 per cent of the realizations that are statistically accepted and physically consistent with the assumptions of the model.

Fig. 6 shows one realization of the selected fits. The other realizations result in comparable fit quality. We show in Table 5 the median value for each of the parameters. The uncertainties shown in this table correspond to the minimum/maximum value obtained for each of the parameters obtained from the 500 fits. We also show in this table the minimum-maximum values of χ^2 for each spin. All values are statistically accepted. Fig. 7 represents the unabsorbed SED models from all the realizations. We show in this figure the total SED in black, the power law component in blue, the reflection component in red, and the disc component in yellow.

All of the best-fitting parameters are consistent for all spins, except the mass and the accretion rate which show a different behaviour. This can be seen in Fig. C2, which shows all the best-fitting parameters for each of the spin values. The figure shows the expected degeneracy between Γ and E_{cut}. In addition it shows a degeneracy between M_{BH}, $\dot{m}/\dot{m}_{Edd}$, and f_{col}. The M_{BH}-$\dot{m}/\dot{m}_{Edd}$ degeneracy is better highlighted in Fig. 8. In this figure, we show each of the best-fitting M_{BH} and $\dot{m}/\dot{m}_{Edd}$ for $a^* = 0$, 0.7, and 0.998 (left-hand, middle, and right-hand panels, respectively). The fact that $\dot{m}$ in physical units is linked to $\dot{m}/\dot{m}_{Edd}$ by the efficiency (η), that is spin dependent, results in obtaining a lower $\dot{m}/\dot{m}_{Edd}$ range as the spin increases, for a given M_{BH}. For a given spin, changing f_{col} results in opposite behavior of M_{BH} and $\dot{m}/\dot{m}_{Edd}$ trying to compensate for the shift in the position of the model peak frequency. This leads to the observed degeneracy between $\dot{m}/\dot{m}_{Edd}$, M_{BH}, and f_{col}. The accretion rate changes between sub- and super-Eddington with f_{col}. For $a^* = 0$, 0.7, and 0.998, $\dot{m}/\dot{m}_{Edd}$ gets below the Eddington limit for f_{col} above 2.2, 1.8, and 1.6, respectively. For most of the possible combinations of parameters the needed M_{BH} value is larger than the one inferred from the width of the optical emission lines reported by Onken et al. (2022). The two values agree within uncertainties for low spin values and low f_{col}. The discrepancy in mass is further discussed in Section 5.3.

Our SED modelling results in a bolometric luminosity that is consistent between all the assumed spins, $L_{bol} = 6.2^{+2.5}_{-0.5} \times 10^{47}$ erg s^{-1}. This is higher than the value of $(4.7 \pm 1.0) \times 10^{47}$ erg s^{-1} obtained by Onken et al. (2022), however, consistent within uncertainties. The measured values of L_{bol} and M_{BH} imply an Eddington ratio of $\lambda_{Edd} = 0.34^{+0.41}_{-0.18}, 0.21^{+0.26}_{-0.12}, 0.11^{+0.15}_{-0.06}$, for $a^* = 0$, 0.7, 0.998, respectively. This is lower than the value of $1.5^{+3.3}_{-1.1}$ implied by Onken et al. (2022), albeit consistent within uncertainties.

4.2 AGNSLIM

As mentioned earlier, accretion discs in super-Eddington AGN are thought to follow a slim disc configuration. For that reason, in this section we fit the SED of J1144 using the AGNSLIM model from Kubota & Done (2019). This model divides the disc in three regions: (a) an inner region (between R_{in} and R_{hot}), where the luminosity is dissipated in hot slab-like material, forming a Comptonized spectrum, (b) an intermediate region (from R_{hot} to R_{warm}) where the luminosity is dissipated in an optically thick and warm Comptonizing medium, and (c) the outer region (from R_{warm} to R_{out}) that is completely thermal emitting a standard blackbody spectrum. This model assumes that the disc extends down to R_{in} with an emissivity following the one of a slim disc. It is worth noting that the slim disc is expected to give a large scale height. However, given the complexity of implementing such geometry, AGNSLIM adopts a geometrically thin disc approximation, and it is limited to modifying the disc emissivity. Furthermore, the model does not include either reprocessing of hard X-rays or general relativity (GR) effects. We define the model in XSPEC parlance as follows:

$$\texttt{Model} = \texttt{redden}_{\rm UV/opt} \times \texttt{TBabs}_{\rm X} \times \texttt{TBpcf}_{\rm X} \times \texttt{AGNSLIM}. \quad (3)$$

Similarly to equation (2), the $redden_{\rm UV/opt}$ component represents the reddening due to Galactic absorption and is applied only to

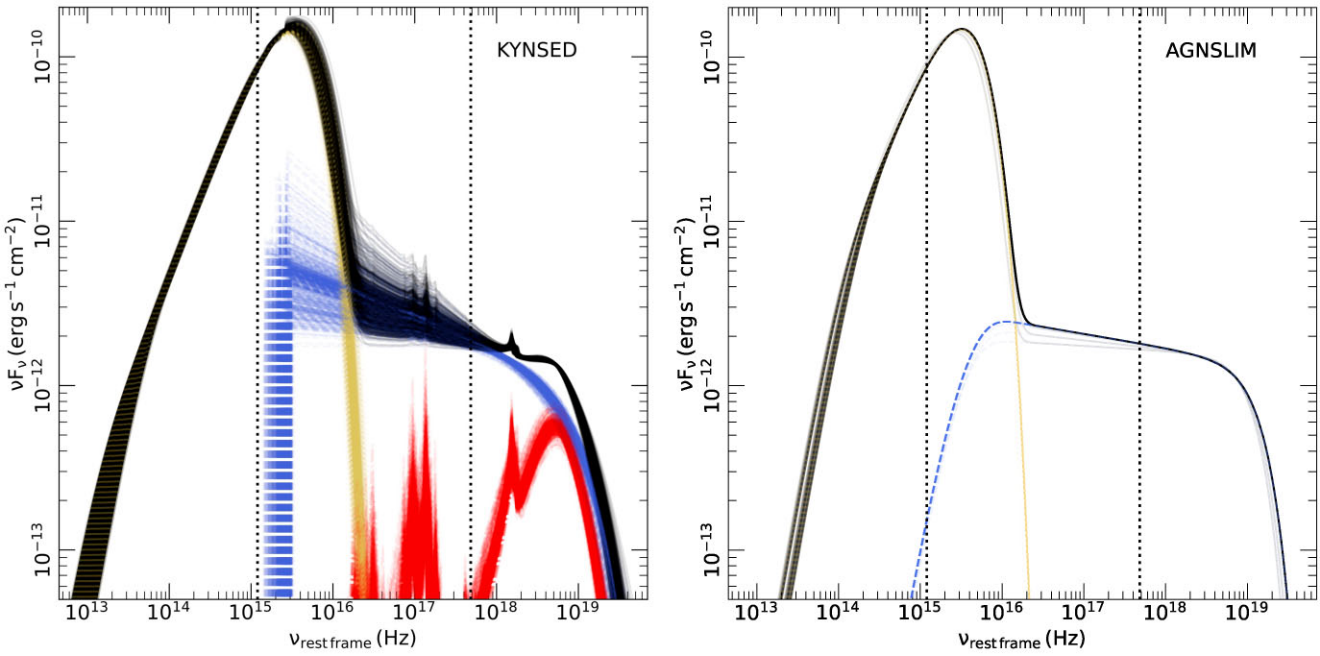

Figure 7. Model SEDs (in the rest frame of the source) obtained from all of the realizations using KYNSED (left) and AGNSLIM (right). The total model is shown in black. The thermal emission of the disc is shown in yellow. The power law component is shown using the dashed blue lines. The dotted red lines correspond to the X-ray reflection from KYNSED (AGNSLIM does not take this component into account). The dotted vertical lines correspond to the intrinsic 2500 Å and 2 keV.

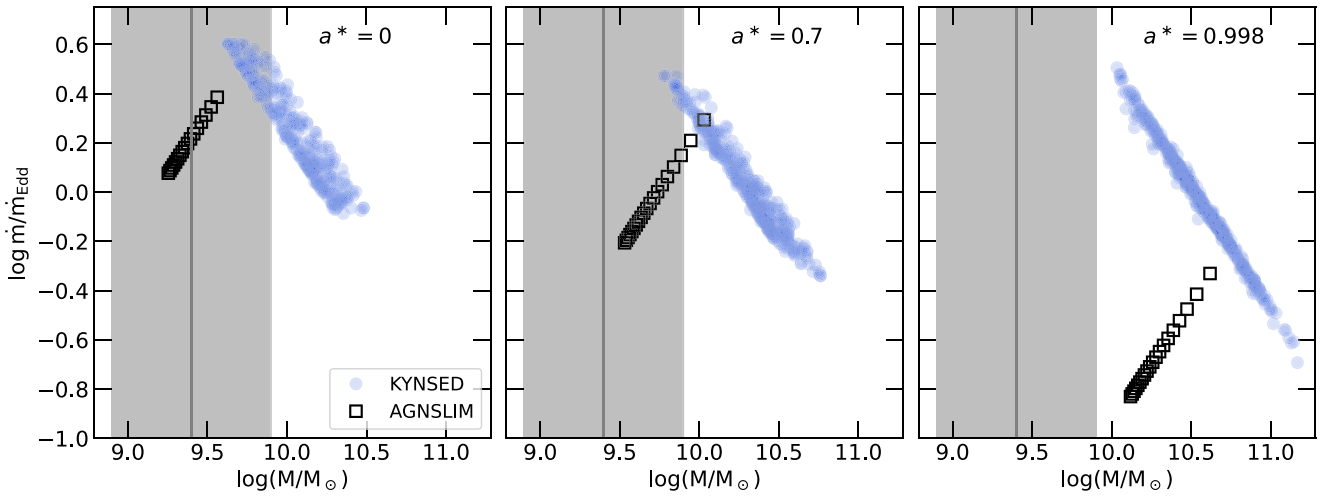

Figure 8. Best-fitting $M_{\rm BH}$ and $\dot{m}/\dot{m}_{\rm Edd}$ obtained by fitting the SED of J1144 assuming $a^* = 0$, 0.7, and 0.998 (left-hand to right-hand panels) using KYNSED (filled circles) and AGNSLIM (open squares). The shaded grey area corresponds to the $M_{\rm BH}$ measurement reported by Onken et al. (2022), using the width of optical emission lines.

the UV/optical data. The $TBabs_{\rm X-ray}$ and $TBpcf_{\rm X-ray}$ components represent the Galactic and intrinsic absorption and they are applied only to the X-ray spectra. We fix $R_{\rm in}$ at its default value of -1, as calculated in equation (1) of Kubota & Done (2019). We assume the outer radius of the disc to be equal to the self-gravity radius as calculated by Laor & Netzer (1989). We fixed the spin values at 0, 0.7, and 0.998. For each spin value, we fixed cosine of the inclination ($\cos\theta$) at 20 values between 0.1 and 1. The free parameters are the BH mass, accretion rate, the temperature ($kT_{\rm h}$), the photon index ($\Gamma_{\rm h}$), and the radius ($R_{\rm h}$) of the hot corona, and the temperature ($kT_{\rm w}$), the photon index ($\Gamma_{\rm w}$), and the radius ($R_{\rm w}$) of the warm corona. The model resulted in statistically good fits, however the warm corona is not needed by the model as its radius always tends to be equal to the one of the hot corona. In fact, this result is expected as the warm corona is usually invoked to explain the presence of a soft X-ray excess (below ~ 1 keV), which is not seen in J1144. We repeated the fit by setting $R_{\rm w} = R_{\rm h}$, thus neglecting the presence of the warm corona. We linked all the parameters for the *XMM-Newton* and *NuSTAR* spectra, except $R_{\rm h}$ which was left free to account for the difference in flux between the two observations. The fits are all acceptable with $\chi^2/{\rm dof} \simeq 277/276$, except for the high inclinations ($\cos\theta \leq 0.2$) of the non-spinning BH case. All of the good fits

Table 6. Best-fitting parameters obtained by modelling the SED of J1144 using AGNSLIM, assuming different values of the spin.

	$a^*=0$	$a^*=0.7$	$a^*=0.998$
$\cos\theta$	$0.2-1$	$0.1-1$	$0.1-1$
$\log \dot{m}/\dot{m}_{\rm Edd}$	$0.18^{+0.21}_{-0.10}$	$-0.08^{+0.37}_{-0.13}$	$-0.70^{+0.37}_{-0.13}$
$\log\ M_{\rm BH}/M_\odot$	$9.36^{+0.20}_{-0.10}$	$9.66^{+0.37}_{-0.13}$	$10.25^{+0.37}_{-0.13}$
$kT_{\rm h}$	16^{+14}_{-5}	16^{+14}_{-5}	16^{+14}_{-5}
$\Gamma_{\rm h}$	$2.09^{+0.04}_{-0.04}$	$2.09^{+0.04}_{-0.04}$	$2.09^{+0.04}_{-0.04}$
$R_{\rm h,\,X}$	$8.96^{+0.19}_{-0.16}$	$4.90^{+0.19}_{-0.16}$	$1.52^{+0.03}_{-0.03}$
$R_{\rm h,\,N}$	$9.58^{+0.31}_{-0.26}$	$5.22^{+0.35}_{-0.31}$	$1.58^{+0.03}_{-0.03}$
$N_{\rm H}$ (10^{22} cm^{-2})	$3.39^{+0.53}_{-0.49}$	$3.39^{+0.53}_{-0.49}$	$3.39^{+0.53}_{-0.49}$
$f_{\rm cov}$	$0.49^{+0.04}_{-0.03}$	$0.49^{+0.04}_{-0.03}$	$0.49^{+0.04}_{-0.03}$
χ^2	277.3	277.3	277.5
dof		276	

The uncertainties on mass and mass accretion rate represent the lowest/highest values obtained from the SED modelling (see text for details). The uncertainties on other parameters correspond to the statistical uncertainty on each of the parameter for a $\Delta\chi^2=1$.

converged to the same value of $\Gamma_{\rm h}$, $kT_{\rm h}$, $N_{\rm H}$, and $f_{\rm cov}$ for all values of spin and inclination. The BH mass and the accretion rate varied with spin and inclination. However, the coronal size varied only as a function of spin. The best-fitting values are shown in Table 6. The uncertainties on mass and mass accretion rate correspond to the lower and upper limits obtained by fitting the SED for different values of $\cos\theta$, for each spin value. The uncertainties on other parameters correspond to the statistical uncertainty on each of the parameter for a $\Delta\chi^2=1$. The right-hand panel of Fig. 6 shows the observed SED fitted with AGNSLIM assuming $a^*=0$. The right-hand panel of Fig. 7 shows the unabsorbed SED models from all the realizations.

Fig. 8 shows how the $M_{\rm BH}$ and $\dot{m}/\dot{m}_{\rm Edd}$ change for different spins. Similarly to the KYNSED model, the increase in spin results in a global increase $M_{\rm BH}$ and decrease in $\dot{m}/\dot{m}_{\rm Edd}$. However, for a given spin value, both $M_{\rm BH}$ and $\dot{m}/\dot{m}_{\rm Edd}$ decrease as $\cos\theta$ increases (see Fig. C3). This is due to the fact that, in AGNSLIM, $\cos\theta$ acts as a normalization factor of the flux, without any effect on the spectral shape. In this case, when $\cos\theta$ changes, both $M_{\rm BH}$ and $\dot{m}/\dot{m}_{\rm Edd}$ adjust to compensate for the change in flux. The best-fitting values of $M_{\rm BH}$ are consistent with the one derived by Onken et al. (2022) for $a^*=0$ and 0.7. A maximally spinning BH results in an $M_{\rm BH}$ larger by an order of magnitude compared to this value. The best-fitting values of BH mass obtained using KYNSED and AGNSLIM are consistent within a factor $\lesssim 2$. However, the accretion rate changes significantly between the two models. This difference increases as the BH spin increases. Since the best-fitting mass and accretion rate correlate with the color correction in KYNSED (see Fig. C2), only the results with $f_{\rm col}=1$ should be considered to compare the results with AGNSLIM. This corresponds to the lowest masses and highest accretion rates for a given spin in KYNSED. In Appendix D, we compare the two models in detail for $\dot{m}/\dot{m}_{\rm Edd}=0.1$ and 1. It is worth noting that, as discussed in Kubota & Done (2019), AGNSLIM is consistent with a standard accretion disc for $\dot{m}/\dot{m}_{\rm Edd}\lesssim 2.39$ which is the case of J1144. AGNSLIM predicts a larger UV emission than KYNSED. The difference increases with spin. This is mainly due to the fact that AGNSLIM does not take into consideration GR effects. Due to GR, a large amount of flux from the inner disc will end up in the BH, hence the difference between the two models. In order to compensate for this, fitting with AGNSLIM results in lower mass and accretion rate compared to KYNSED. For the non-spinning case, AGNSLIM results in an accretion rate above the Eddington limit but below the critical limit of $\sim 2.39\,\dot{m}_{\rm Edd}$. For $a^*=0.7$, $\dot{m}/\dot{m}_{\rm Edd}$ gets below the Eddington limit for $\cos\theta>0.4$. The maximally spinning case results in a sub-Eddington accretion rate for all cases. We note that this modelling also predicts a compact X-ray corona located within $10\,r_{\rm g}$ of the BH for all spin values. The value of $R_{\rm h}$ decreases by increasing the spin.

We derive from this model a bolometric luminosity $L_{\rm bol}=6.00^{+0.11}_{-0.04}\times10^{47}$ erg s^{-1}, consistent with the value derived from the KYNSED modelling. The measured values of $L_{\rm bol}$ and $M_{\rm BH}$ imply an Eddington ratio of $\lambda_{\rm Edd}=2.08^{+0.56}_{-0.78}$, $1.04^{+0.36}_{-0.60}$, and $0.27^{+0.09}_{-0.16}$, for $a^*=0$, 0.7, and 0.998, respectively. If the BH spin were low/intermediate, this would imply a super-Eddington accretion rate consistent with the value derived by Onken et al. (2022).

5 DISCUSSION

We have presented in this work the results from X-ray observations of J1144, the most luminous QSO in the last ~ 9 Gyr, using eROSITA, *Swift*, *XMM-Newton*, and *NuSTAR*. Despite the fact that the source was not detected by ROSAT, it is currently detected by all of the observatories showing an X-ray variability by a factor of $\sim$10 within a year. We also detected a shorter time-scale variability of the order of $\sim$2.7 within $\sim$40 d. The X-ray spectrum of this source can be well described using an absorbed power law with a high-energy cutoff. We also modelled the broadband SED of the source. Both a standard accretion disc irradiated by a point-like X-ray source, and a slim-disc emissivity profile could fit the observed SED equally well. This resulted in a bolometric luminosity of $6.2^{+2.5}_{-0.5}\times10^{47}$ erg s^{-1} ($6.00^{+0.11}_{-0.04}\times10^{47}$ erg s^{-1}) using KYNSED (AGNSLIM). This makes it the brightest QSO for $z\lesssim 1.3$, and among the most luminous 0.1 per cent known QSOs.

5.1 X-ray properties

5.1.1 Coronal properties

The X-ray spectrum of this source is consistent with a power law with a high-energy cutoff. Due to the quality of the data, we assumed that the photon index is constant for all the eRASS observations, and also constant during the recent monitoring in 2022. The photon indices from the two epochs are consistent within uncertainties suggesting a rather soft spectrum. Thanks to the *NuSTAR* observation, we are able to measure the high-energy cutoff. The measured value of $E_{\rm cut}$ depends on the employed model. For a simple absorbed power law we found $E_{\rm cut}=68^{+65}_{-23}$ keV. However, when a reflection component is added this value reaches 23^{+13}_{-6} keV. This is due to the fact that the latter model assumes that part of the curvature in the hard X-rays is also due to the presence of the Compton hump (see left-hand panel of Fig. 7), which shifts $E_{\rm cut}$ to a lower value. However, in both cases $E_{\rm cut}$ is one of the lowest measured in AGN (see e.g. Kara et al. 2017; Reeves et al. 2021). When placed in the $L_{\rm X}$–$E_{\rm cut}$ plane, the source falls well in the limited region allowed to avoid runaway pair production, at its corresponding X-ray luminosity (e.g. Fabian et al. 2015, 2017; Lanzuisi et al. 2019). This may suggest that the corona of J1144 is a pair dominated hybrid plasma (see Fabian et al. 2017).

Using equations (2)–(5)[5] from Middei et al. (2019), we mapped our results from the Γ–$E_{\rm cut}$ plane in the kT–τ plane. We used the

[5]We note that a minus sign is missing from equation (5) in Middei et al. (2019). The correct expression is $\beta(\tau)=-3.35+1.3\tau-0.11\tau^2$.

Table 7. Bolometric luminosity, unabsorbed 2–10 keV luminosity, the optical-to-X-ray ratio (α_{ox}), and the Eddington ratio obtained by modelling the SED of J1144.

	KYNSED				AGNSLIM			
	$a^* = 0$	$a^* = 0.7$	$a^* = 0.998$	All	$a^* = 0$	$a^* = 0.7$	$a^* = 0.998$	All
L_{bol} (10^{47} erg s^{-1})	$6.19^{+0.58}_{-0.33}$	$6.20^{+0.81}_{-0.34}$	$6.26^{+1.37}_{-0.45}$	$6.21^{+1.42}_{-0.38}$	$5.97^{+0.01}_{-0.01}$	$6.00^{+0.01}_{-0.01}$	$6.10^{+0.01}_{-0.01}$	$6.00^{+0.11}_{-0.04}$
L_{2-10} (10^{45} erg s^{-1})	$5.11^{+0.47}_{-0.29}$	$5.09^{+0.49}_{-0.28}$	$5.08^{+0.52}_{-0.31}$	$5.09^{+0.51}_{-0.32}$	$4.99^{+0.01}_{-0.01}$	$4.99^{+0.01}_{-0.01}$	$4.99^{+0.01}_{-0.01}$	$4.99^{+0.01}_{-0.01}$
α_{ox}	$-1.63^{+0.04}_{-0.02}$	$-1.63^{+0.04}_{-0.02}$	$-1.64^{+0.04}_{-0.03}$	$-1.63^{+0.04}_{-0.03}$	$-1.65^{+0.01}_{-0.01}$	$-1.65^{+0.01}_{-0.01}$	$-1.65^{+0.01}_{-0.01}$	$-1.65^{+0.01}_{-0.01}$
λ_{Edd}	$0.39^{+0.75}_{-0.23}$	$0.23^{+0.57}_{-0.14}$	$0.14^{+0.30}_{-0.11}$	$0.22^{+0.92}_{-0.19}$	$2.08^{+0.56}_{-0.78}$	$1.04^{+0.36}_{-0.60}$	$0.27^{+0.09}_{-0.16}$	$0.97^{+1.66}_{-0.85}$

We show the values obtained assuming different spin values. We also show the results for all spins together. Similar to Table 5, the uncertainties represent the lowest/highest values obtained from the SED modelling.

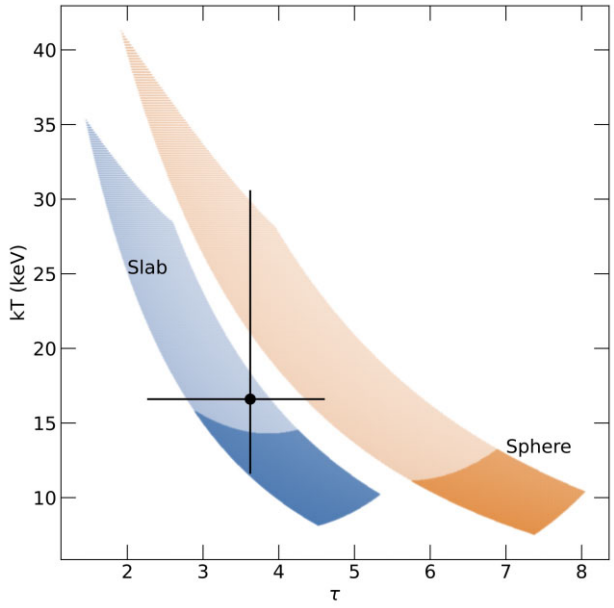

Figure 9. Electron temperature (kT) vs optical depth (τ) of the corona obtained by assuming Comptonization and mapping the Γ–E_{cut} plane into this plane, following Middei et al. (2019). We assumed a slab and spherical geometry (blue and orange, respectively). The darker regions correspond to the limits if E_{cut} is obtained from the KYNSED model. The lighter regions are obtained by extending the upper limit of E_{cut} to 70 keV, as a conservative limit, to match the results obtained from fitting a simple power law with a high-energy cutoff model. The black circle correspond to the estimates of kT and τ obtained from fitting the SED with AGNSLIM, which assumes a slab geometry.

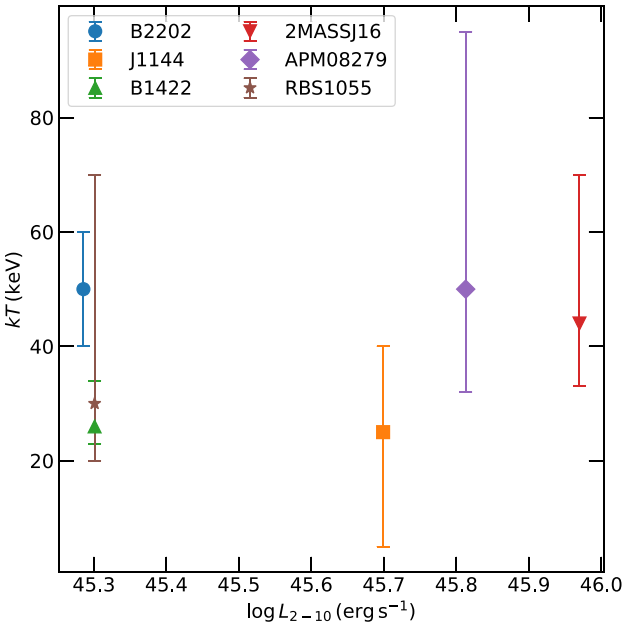

Figure 10. Comparison of J1144 to other quasars from the literature, with $L_{2-10} > 10^{45}$ erg s^{-1}, in the $kT - L_{2-10}$ plane.

results from modelling the broadband SED, with Γ in the range 2–2.4 and E_{cut} in the range 15–70 keV, assuming a slab and a spherical geometry of the corona. We consider a conservative upper limit on E_{cut} to take into account the value measured using a simple power-law model. The results are shown in Fig. 9. For a slab geometry, we find τ in the range 1.5–5.4 and kT in the range $5 - 35$ keV. For a spherical geometry, we find τ in the range 2–8 and kT in the range $7 - 40$ keV. We also used the best-fitting temperature and photon index derived from AGNSLIM ($kT = 16^{+14}_{-5}$ keV, $\Gamma = 2.09 \pm 0.04$), which assumes a slab geometry, to derive the optical depth. Using equation (2) of Middei et al. (2019), we obtain $\tau = 3.6^{+1.0}_{-1.4}$ (we considered the uncertainty on kT only). These values of kT and τ are in agreement with the ones derived from KYNSED (see Fig. 9). Our results add another QSO to the highly accreting sources with a low coronal temperature (e.g. Ark 564 and PDS 456 Kara et al. 2017; Reeves et al. 2021). More recently, Tortosa et al. (2023) also found low temperatures in two rapidly accreting AGN Mrk 382, IRAS 04416 + 1215. In Fig. 10, we compare J1144 to other sources with $L_{2-10} > 10^{45}$ erg s^{-1}, namely: B2202–209 (Kammoun et al. 2017), 2MASS J1614346+470420 and B1422 + 231 (Lanzuisi et al. 2019), APM 08279 + 5255 (Bertola et al. 2022), and RBS 1055 (Marinucci et al. 2022). The coronal temperature in J1144 is broadly consistent with these sources, being among the lowest. We note also that, as mentioned earlier, the two models used in this work provide an estimate of the size of the X-ray corona. The measured sizes are listed in Tables 5–6. Both models predict a compact corona with radius smaller than $\sim 10\,r_g$ (KYNSED gives an upper limit of $25\,r_g$).

Various works have presented a positive correlation between the photon index and the Eddington ratio in QSOs (e.g. Shemmer et al. 2008; Risaliti, Young & Elvis 2009; Brightman et al. 2013; Liu et al. 2021). This correlation is usually explained by the fact that at high Eddington ratios the UV/optical emission from the accretion disc is enhanced which leads to a more efficient Compton cooling of the corona, decreasing kT, which leads to a softening of the X-ray spectrum (an increase in the photon index). Fig. 11 shows Γ versus $\log \lambda_{Edd}$ for the different spin values considered in this work using KYNSED and AGNSLIM. We compare these results to the data obtained by Liu et al. (2021). J1144 is consistent with the observed Γ–$\log \lambda_{Edd}$ correlation, for both models and all spin values.

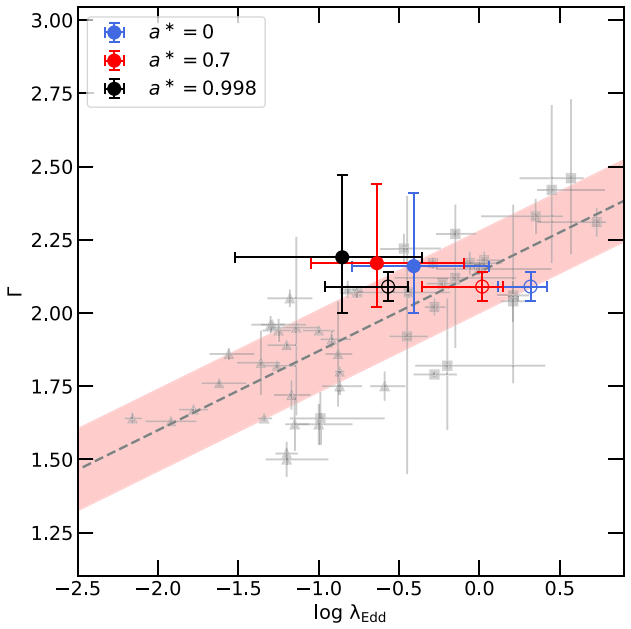

Figure 11. Photon index versus Eddington ratio assuming $a^* = 0$, 0.7, and 0.998 (blue, red, and black, respectively). Filled and open circles correspond to the results obtained using KYNSED and AGNSLIM, respectively. Triangles and squares correspond to the data from Liu et al. (2021) for sub- and super-Eddington sources, respectively. The dashed line and the shaded area represent the best-fitting to the Liu et al. (2021) data and the corresponding 1σ scatter, respectively.

5.1.2 X-ray reflection

No strong signature of the presence of reflection can be inferred from the current spectra. However, as mentioned in Appendix A, including an emission line at ~ 6.5 keV improves the fit by $\Delta\chi^2 \simeq -9$. The equivalent width of the line (EW $= 117 \pm 44$ eV) is in agreement with the expected one, of 150 eV, for solar abundance and a 2π covering (George & Fabian 1991). We note that this value is larger than the one expected from the Iwasawa–Taniguchi effect (see e.g. Iwasawa & Taniguchi 1993; Bianchi et al. 2007) for the luminosity of this source. Similar large equivalent widths have also been seen in a few powerful QSOs (e.g. Krumpe et al. 2010; Marinucci et al. 2022).

KYNSED includes a disc reflection component with a self-consistently calculated ionization profile. The model provides the ionization parameter ($\xi_{\rm in}$) at the inner edge of the disc as an output. These values are listed in Table 5. The model suggests a low ionization state of the disc, consistent with neutral, for all of the spin values. In order to estimate the importance of reflection in the model, we calculate the ratio of the reflection component to the power law component for each of the fits in the $1.6 - 16$ keV observed range (equivalent to $3 - 30$ keV, rest frame). Then, to compare this ratio to the commonly used reflection fraction ($\mathcal{R}$) we used the relation between this flux ratio and $\mathcal{R}$ derived in fig. 9 of Kammoun et al. (2020), for neutral reflection:

$$\log \mathcal{R} = (1.38 \pm 0.18) \log \left(\frac{F_{\rm ref}}{F_{\rm PL}} \right)_{3-30} + (0.65 \pm 0.06). \quad (4)$$

This results in $\mathcal{R} = 0.82^{+0.66}_{-0.27}$ considering all the spin values. The values of $\mathcal{R}$ for each spin are shown in Table 5. We tested the reflection spectrum by modelling the *XMM-Newton* and *NuSTAR* spectra only using Relxill (Dauser et al. 2013, 2016). This gives consistent results with the modelling using KYNSED. The best-fitting photon index, cutoff energy, and reflection fraction are $\Gamma = 2.17 \pm 0.13$, $E_{\rm cut} = 48^{+33}_{-11}$ keV, and $\mathcal{R} = 1.2^{+1.1}_{-0.8}$. Deeper exposures are required to confirm the presence of the reflection with a higher confidence.

It is worth noting that no soft X-ray excess has been seen in this source. In particular, the spectrum in eRASS1, when the source was at its highest flux with low intrinsic absorption, is consistent with a simple power law. This, interestingly, rules out the presence of any strong soft component in J1144.

5.1.3 X-ray to UV/optical ratio

Comparing the X-ray to the bolometric luminosity inferred from the broadband SED modelling we find a $L_{\rm bol}/L_{2-10} \sim 120$. Such a large value is typically seen in bright QSO (e.g. Lusso et al. 2012; Duras et al. 2020). We measured the unabsorbed specific luminosity at 2500 Å and 2 keV, using the best-fitting SED models. For comparison, we plot, in the left-hand panel of Fig. 12, $\log L_{\rm 2keV}$ vs $\log L_{2500\text{Å}}$ from Lusso et al. (2020) in grey. We fitted these data with a straight line using the ordinary least square method (OLS(Y|X); Isobe et al. 1990). The black solid line corresponds to the best-fitting line. J1144 agrees well with this relation within 1σ (red shaded area). We also estimated the X-ray to UV ratio, defined as $\alpha_{\rm ox} = 0.3838 \log \left(L_{\rm 2keV}/L_{2500\text{Å}} \right)$, to be $-1.64^{+0.06}_{-0.04}$ (-1.65 ± 0.01) using KYNSED (AGNSLIM). The right-hand panel of Fig. 12 shows $\alpha_{\rm ox}$ vslog $L_{2500\text{Å}}$, also from Lusso et al. (2020). We also fit a straight line to the relation, and we find that J1144 agrees with it within 1σ. Considering the intrinsic absorption will result in $\alpha_{\rm ox} = -1.7$, still consistent with the Lusso et al. (2020) results. In addition, we estimated $\alpha_{\rm ox}$ during the *Swift* monitoring. We used the UVOT/M2 filter to scale $L_{2500\text{Å}}$ and considered the observations where XRT and UVOT/M2 data are available (XRT/O1, O9, and O10). The estimated values of $\alpha_{\rm ox}$ are shown as black connected circles in Fig. 12. Interestingly, in all these observations, the source never reaches an X-ray weak state,[6] contrary to other variable high-Eddington sources (see e.g. Laurenti et al. 2021).

5.2 Outflow signature

The X-ray spectra of the source do not show any evidence of absorption by winds or ultra fast outflows. The absorption line detected at ~ 1.3 keV could be due to some intrinsic absorbing material. However, identifying the origin of this line is hard. Similar features can also be seen in the eROSITA (eRASS2 and eRASS5) and *Swift*/XRT spectra. The quality of the data does not allow us to confirm the existence of these features with high confidence. However, the 'transient-like' aspect of these features could hint at an outflowing origin.

Fabian, Celotti & Erlund (2006), Fabian, Vasudevan & Gandhi (2008), and Fabian et al. (2009) discussed that, in the presence of dust, the gas couples with the dust grains via Coulomb interaction and the cross-section for the interaction with photons is enhanced. Thus, the effective Eddington limit, for which the outward radiation pressure on gas exceeds the inward gravitational pull, is much lower for dusty gas than for ionized dust-free gas (e.g. Laor & Draine 1993; Scoville & Norman 1995). This implies that AGN considered as sub-Eddington using the standard definition may nevertheless exceed the

[6] X-ray weakness is usually estimated using $\Delta\alpha_{\rm ox}$ which is the difference between the estimated and the predicted $\alpha_{\rm ox}$ for a given luminosity. Sources with $\Delta\alpha_{\rm ox} \leq -0.3$ can be reasonably classified as X-ray weak.

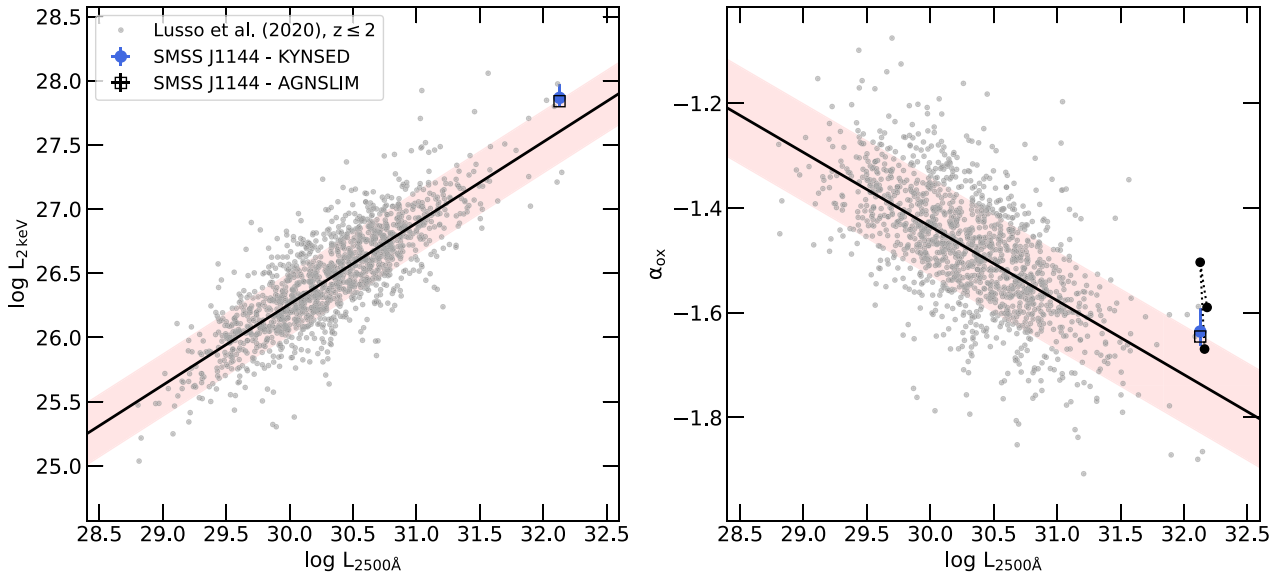

Figure 12. $L_{2\,\mathrm{keV}}$ vs $L_{2500\text{Å}}$ (left) and α_{ox} vs $L_{2500\text{Å}}$ (right) for the QSOs at $z \leq 2$ presented in Lusso et al. (2020; grey dots). The solid line represents the best-fitting straight line to these data. The red shaded area represents the 1σ scatter around the best-fitting model. The estimates of J1144 from the SED fitting are shown as a blue circle for KYNSED and as a empty black square for AGNSLIM. The black connected circles show the variability of α_{ox} during the *Swift* monitoring (see Section 5.1.3 for details).

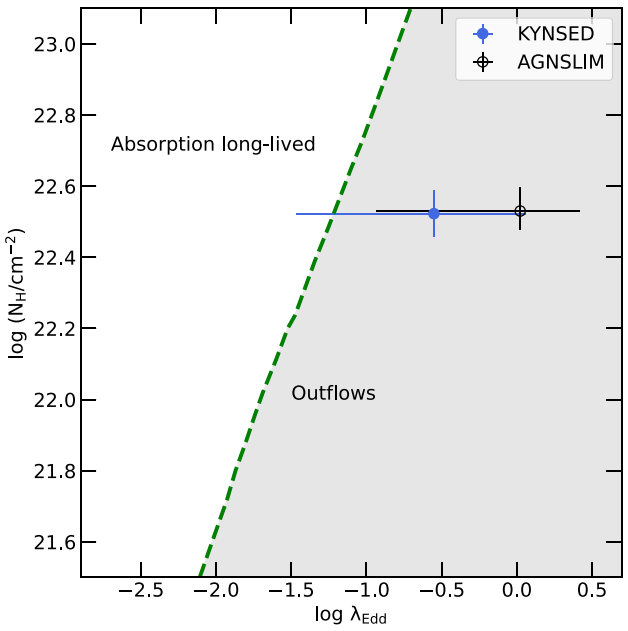

Figure 13. Intrinsic absorption column density versus the Eddington ratio obtained from modelling the SED of J1144 using KYNSED (blue circle) and AGNSLIM (black empty square). The green dashed line shows the effective Eddington limit above which dusty clouds (with standard ISM grain abundance; adapted from Fabian et al. 2009) see the AGN as being effectively above the Eddington limit. Long-lived absorbing clouds can only occur for N_{H} above this line. J1144 falls within the outflow region shown in grey.

effective Eddington limit for substantial column densities of dusty gas. In this case, long-lived, stable clouds can survive radiation pressure only in a regime lower than the effective Eddington limit. Otherwise, the gas seeing the nucleus above the effective Eddington limit is expelled, and should be experiencing outflows. In this case absorption may be transient or variable. Fabian et al. (2008, 2009) used CLOUDY to derive a limit between the long-lived and the outflow absorption in the N_{H}–λ_{Edd} plane. This limit is shown in Fig. 13. J1144 resides on the right-hand side of that limit, suggesting that the absorption in this source is due to outflow. The fact, that the absorption measured from the eROSITA spectra is much lower than the one measured during the more recent monitoring by more than an order of magnitude supports this hypothesis, as this absorption is expected to be variable. Furthermore, our modelling of the SED requires a partial covering of the X-ray source without any additional absorption for the UV/optical. This could indicate that this absorption is located closer to the BH, and is of an outflow origin. Baskin & Laor (2018) estimated the inner disc radius ($R_{\mathrm{in}} = 0.018 L_{46}^{0.5}$ pc, where L_{46} is the bolometric luminosity in units of 10^{46} erg s^{-1}) which can have a dusty atmosphere, so dusty wind could be launched at a distant between R_{in} and the sublimation radius. This results in $R_{\mathrm{in}} = 0.04$ pc. Considering log $M_{\mathrm{BH}}/\mathrm{M}_{\odot}$ between 9.5 and 11, we estimate R_{in} to be between $\sim 30 - 900\, r_{\mathrm{g}}$. Supporting further the possibility of the absorption being connected to disc winds. Better quality data are needed to confirm this. High quality X-ray and UV/optical spectra will be crucial to detect the possible presence of outflows in this source, and to study the variability of absorption. In particular, the next generation of X-ray microcalorimeter like *XRISM*/Resolve (Tashiro et al. 2018) and *Athena*/X-IFU (Barret et al. 2023) will unveil more secrets about this and other sources at comparable redshift. This will help us to better understand the evolution of such massive and rapidly accreting black holes.

5.3 Black hole mass

The inferred BH mass depends strongly on the assumed SED model. An X-ray illuminated standard accretion disc predicts higher mass values compared to a model assuming a slim disc emissivity profile, which gives a mass estimate closer to the single-epoch value obtained by measuring line width in Onken et al. (2022). In fact, the single-

epoch mass estimates are subject to various biases and uncertainties (e.g. Shen 2013). In particular, the virialized masses estimated are thought to be underestimated in sources like J1144, where radiation pressure is important (Marconi et al. 2008, 2009). It is also worth noting that the relations used by Onken et al. (2022) represent an extrapolation by almost an order of magnitude in luminosity compared to the Hβ reverberation mapping sample of Bentz et al. (2013). Thus, it may be plausible that the true mass of the source is larger than the value estimated by Onken et al. (2022).

Both models used in this work predict a relatively large mass for a spinning BH. It is also worth noting that, although `AGNSLIM` adopts a slim disc emissivity profile, it has several assumptions that could affect the measured $M_{\rm BH}$. For instance, the model neglects all the GR effects which could alter emission from the innermost regions of the system, especially for sources where the corona is quite compact similar to J1144. In addition, `AGNSLIM` does not account properly for the inclination of the system that could affect the spectral shape (not only the overall flux; see fig. A6 in Dovčiak et al. 2022). It also neglects the presence of any reprocessing of the X-rays by the disc, which could affect the X-ray spectrum as well as the disc emission by heating its surface (see Kammoun et al. 2021b; Dovčiak et al. 2022). As for `KYNSED`, the BH mass inferred from this model is highly affected by the assumed value of $f_{\rm col}$. However, the true value of $f_{\rm col}$ is quite uncertain, and depends itself on the BH mass and accretion rate (see e.g. Davis & El-Abd 2019).

The current data do not allow us to distinguish between the two models. However, the source is confirmed to be in the high-mass regime with $\log\ M_{\rm BH}/{\rm M}_{\odot} \gtrsim 9.5$. King (2016) estimated the maximum physical limit of mass that an SMBH can reach through luminous accretion of gas as a function of the BH spin (see their fig. 1). All of the estimated values of the BH mass in J1144 (using both models) lie below this limit. We note that, in all cases, the main conclusions of our work will not be strongly affected by the exact value of $M_{\rm BH}$.

5.4 Variability

As mentioned earlier, the ROSAT upper limit is consistent with the low-flux state seen in the data presented in this paper. Moreover, we used HILIGT to derive upper limits for the *XMM-Newton* Slew catalogue. These limits are not very constraining as they are consistent with the high-flux state of the source. Thus, we cannot conclude on the X-ray variability of the source over a time-scale of a couple of decades. In other terms, we cannot confirm whether the ROSAT non-detection is due to an intrinsic X-ray weakness of the source or due to the flux limit of the observations.

On the shorter time-scales, in addition to the variability seen in absorption, the source also exhibits intrinsic flux changes on time-scales of days to years that could reach a factor of $\sim$10 as seen in the eROSITA data. The shortest max-to-min change seen during the monitoring of the source is of the order of 2.7 over $\sim$17 d (observed). Based on the `KYNSED` results, this would correspond to $\sim$1.6–24.6 times the light-crossing time per gravitational radius ($t_{\rm cross} = GM_{\rm BH}/c^3$), in the rest frame of the source after correcting for time dilation due to the cosmological redshift. This would increase up to $\sim 66\, t_{\rm cross}$ for $\log\ M_{\rm BH}/{\rm M}_{\odot} = 9.4$. The range is quite uncertain due to the uncertainty on the mass. However, in all cases, this variability time-scale is longer than the light crossing time. Thus, the X-ray variability could simply originate from intrinsic changes in the luminosity of the X-ray corona. A lower amplitude variability is also seen in the in the UV/optical range. While this is very unlikely due to intrinsic changes in the accretion disc, the observed variability may be well driven by thermal reverberation as the disc responds to the X-ray variability (e.g. Kammoun et al. 2021b). It is worth noting that the quality of the data does not allow us to constrain any spectral changes that could occur in the source. Addressing all these points requires a more intense monitoring campaign and deeper observations in X-ray/UV/optical.

6 CONCLUSION

In this paper we analysed the X-ray spectra of J1144 from five eROSITA observations performed between the end of 2019 and the end of 2021. In addition, we analyse the results obtained from a recent monitoring of the source using *Swift*, *XMM-Newton*, and *NuSTAR*. The source shows a large X-ray variability that is due to intrinsic changes in the X-ray luminosity of the source accompanied with changes in the absorption in the line of sight. This absorption could be due to a radiatively driven outflow material. The observed SED of J1144 could be fitted equally with a standard accretion disc around a BH with a mass of a few times $10^{10}\ M_{\odot}$, and with a slim disc model assuming a smaller BH mass of the order of a few times 10^9 $M_{\odot}$. In both cases, the source seems to accrete at a rate larger than 40 per cent of the Eddington limit. If we assume a low BH spin the accretion rate can even exceed the Eddington limit. Assuming a Comptonization model, we measure the coronal electron temperature to be of the order of $\sim$10–40 keV. With a bolometric luminosity of 6.2×10^{47} erg s^{-1}, this source is the most luminous QSO in the last 9 Gyr. Interestingly, the optical-X-ray properties of the source are different than many high-Eddington sources. Notably, the measured $\alpha_{\rm ox}$ value is consistent with standard radio-quiet QSOs rather than high-Eddington QSOs which tend to be X-ray weak. This could hint towards a sub-Eddington accretion rate, thus a non-zero BH spin and a large mass. Moreover, the source shows a hint of an Fe Kα line with an equivalent width of 117 ± 44 eV, that is larger than what is expected for sources with a similar X-ray luminosity. Modelling the SED by including an X-ray reflection results in a reflection fraction of the order of unity.

Further deeper X-ray and UV/optical observations are needed to measure more accurately the nature of the absorption in this source and its variability. In addition, this will help confirm the presence of absorption features in the soft X-rays, check for further signatures of outflow, and better understand the origin of the large variability seen in this source. These observations will give us a glimpse at what happens in very luminous QSOs at cosmic noon, while requiring moderate observing time. This will allow us to better understand the growth of such massive black holes and study the connection between the activity of the central engine and its environment.

ACKNOWLEDGEMENTS

We thank the PI of *NuSTAR*, Fiona A Harrison, the Project Scientist of *XMM-Newton*, Norbert Schartel, and the PI of *Swift*, Brad Cenko, as well as the planning staff of the three observatories for making these observations possible.

This research is based on observations obtained with *XMM-Newton*, an ESA science mission with instruments and contributions directly funded by ESA Member States and NASA. This research made use of data from the *NuSTAR* mission, a project led by the California Institute of Technology, managed by the Jet Propulsion Laboratory, and funded by NASA. This research made use of Astropy, a community-developed core PYTHON package for Astronomy (Astropy Collaboration 2018), 2013. This research made use of SCIPY (Virtanen et al. 2020). This research made use of NUMPY (Harris et al.

2020). This research made use of matplotlib, a PYTHON library for publication quality graphics (Hunter 2007). This research made use of XSPEC (Arnaud 1996). We acknowledge the use of public data from the *Swift* data archive.

This work is based on data from eROSITA, the soft X-ray instrument aboard SRG, a joint Russian-German science mission supported by the Russian Space Agency (Roskosmos), in the interests of the Russian Academy of Sciences represented by its Space Research Institute (IKI), and the Deutsches Zentrum für Luft- und Raumfahrt (DLR). The SRG spacecraft was built by Lavochkin Association (NPOL) and its subcontractors, and is operated by NPOL with support from the Max Planck Institute for Extraterrestrial Physics (MPE). The development and construction of the eROSITA X-ray instrument was led by MPE, with contributions from the Dr Karl Remeis Observatory Bamberg & ECAP (FAU Erlangen-Nuernberg), the University of Hamburg Observatory, the Leibniz Institute for Astrophysics Potsdam (AIP), and the Institute for Astronomy and Astrophysics of the University of Tübingen, with the support of DLR and the Max Planck Society. The Argelander Institute for Astronomy of the University of Bonn and the Ludwig Maximilians Universität Munich also participated in the science preparation for eROSITA. The eROSITA data shown here were processed using the eSASS/NRTA software system developed by the German eROSITA consortium.

ESK, DB, and POP acknowledge financial support from the Centre National d'Etudes Spatiales (CNES). ZI acknowledges funding from the ORIGINS cluster funded by the Deutsche Forschungsgemeinschaft (DFG, German Research Foundation) under Germany's Excellence Strategy – EXC-2094–390783311. POP and SB acknowledge financial support from the French National High Energy Program (PNHE) of CNRS. EP acknowledges financial support from PRIN MIUR project 'Black Hole winds and the Baryon Life Cycle of Galaxies: the stone-guest at the galaxy evolution supper', contract #2017PH3WAT.

We thank the referee, Chris Done, for her useful comments and discussions about AGNSLIM. We thank Riccardo Middei for clarifications about the results from the MoCA code.

DATA AVAILABILITY

The *Swift*, *XMM-Newton*, and *NuSTAR* data are all available on the archives corresponding to each of the observatories. Data from eRASS1 are planned to be publicly released in Spring 2023, with the rest of the eROSITA data used in this paper (eRASS2–5) being made available 2 yr later.

REFERENCES

Abramowicz M. A., Czerny B., Lasota J. P., Szuszkiewicz E., 1988, ApJ, 332, 646
Arnaud K. A., 1996, in Jacoby G. H., Barnes J. eds, ASP Conf. Ser. Vol. 101, Astronomical Data Analysis Software and Systems V. Astron. Soc. Pac., San Francisco. p. 17
Astropy Collaboration, 2018, AJ, 156, 123
Barret D. et al., 2023, Exp. Astron.
Baskin A., Laor A., 2018, MNRAS, 474, 1970
Bentz M. C. et al., 2013, ApJ, 767, 149
Bertola E. et al., 2022, A&A, 662, A98
Bianchi S., Guainazzi M., Matt G., Fonseca Bonilla N., 2007, A&A, 467, L19
Bohlin R. C., Savage B. D., Drake J. F., 1978, ApJ, 224, 132
Brightman M. et al., 2013, MNRAS, 433, 2485
Brunner H. et al., 2022, A&A, 661, A1
Buchner J., 2021a, J. Open Source Softw., 6, 3001
Buchner J., 2021b, J. Open Source Softw., 6, 3045
Buchner J. et al., 2014, A&A, 564, A125
Buchner J., Boller T., Bogensberger D., Malyali A., Nandra K., Wilms J., Dwelly T., Liu T., 2022, A&A, 661, A18
Burrows D. N. et al., 2005, Space Sci. Rev., 120, 165
Castelló-Mor N. et al., 2017, MNRAS, 467, 1209
Chartas G., Kochanek C. S., Dai X., Poindexter S., Garmire G., 2009, ApJ, 693, 174
Dauser T., Garcia J., Wilms J., Böck M., Brenneman L. W., Falanga M., Fukumura K., Reynolds C. S., 2013, MNRAS, 430, 1694
Dauser T., García J., Walton D. J., Eikmann W., Kallman T., McClintock J., Wilms J., 2016, A&A, 590, A76
Davis S. W., El-Abd S., 2019, ApJ, 874, 23
Dovčiak M., Done C., 2016, Astron. Nachr., 337, 441
Dovčiak M., Papadakis I. E., Kammoun E. S., Zhang W., 2022, A&A, 661, A135
Duras F. et al., 2020, A&A, 636, A73
Fabian A. C., Celotti A., Erlund M. C., 2006, MNRAS, 373, L16
Fabian A. C., Vasudevan R. V., Gandhi P., 2008, MNRAS, 385, L43
Fabian A. C., Vasudevan R. V., Mushotzky R. F., Winter L. M., Reynolds C. S., 2009, MNRAS, 394, L89
Fabian A. C., Lohfink A., Kara E., Parker M. L., Vasudevan R., Reynolds C. S., 2015, MNRAS, 451, 4375
Fabian A. C., Lohfink A., Belmont R., Malzac J., Coppi P., 2017, MNRAS, 467, 2566
Gabriel C. et al., 2004, in Ochsenbein F. , Allen M. G. , Egret D. eds, ASP Conf. Ser. Vol. 314, Astronomical Data Analysis Software and Systems (ADASS) XIII. Astron. Soc. Pac., San Francisco. p. 759
George I. M., Fabian A. C., 1991, MNRAS, 249, 352
Giustini M., Proga D., 2019, A&A, 630, A94
Gordon C. , Arnaud K. , 2021, Astrophysics Source Code Library, record ascl:2101.014
HI4PI Collaboration, 2016, A&A, 594, A116
Haardt F., Maraschi L., 1993, ApJ, 413, 507
Haardt F., Maraschi L., Ghisellini G., 1994, ApJ, 432, L95
Harris C. R. et al., 2020, Nature, 585, 357
Hunter J. D., 2007, Comput. Sci. Eng., 9, 90
Isobe T., Feigelson E. D., Akritas M. G., Babu G. J., 1990, ApJ, 364, 104
Iwasawa K., Taniguchi Y., 1993, ApJ, 413, L15
Johnson J. L., Haardt F., 2016, PASA, 33, e007
Kammoun E. S. et al., 2017, MNRAS, 465, 1665
Kammoun E. S., Papadakis I. E., Dovčiak M., 2019, ApJ, 879, L24
Kammoun E. S. et al., 2020, ApJ, 901, 161
Kammoun E. S., Papadakis I. E., Dovčiak M., 2021a, MNRAS, 503, 4163
Kammoun E. S., Dovčiak M., Papadakis I. E., Caballero-García M. D., Karas V., 2021b, ApJ, 907, 20
Kara E., Alston W. N., Fabian A. C., Cackett E. M., Uttley P., Reynolds C. S., Zoghbi A., 2016, MNRAS, 462, 511
Kara E., García J. A., Lohfink A., Fabian A. C., Reynolds C. S., Tombesi F., Wilkins D. R., 2017, MNRAS, 468, 3489
King A., 2016, MNRAS, 456, L109
King A., Pounds K., 2015, ARA&A, 53, 115
Krumpe M., Lamer G., Markowitz A., Corral A., 2010, ApJ, 725, 2444
Kubota A., Done C., 2018, MNRAS, 480, 1247
Kubota A., Done C., 2019, MNRAS, 489, 524
Lanzuisi G. et al., 2019, ApJ, 875, L20
Laor A., Draine B. T., 1993, ApJ, 402, 441
Laor A., Netzer H., 1989, MNRAS, 238, 897
Laurenti M., Luminari A., Tombesi F., Vagnetti F., Middei R., Piconcelli E., 2021, A&A, 645, A118
Laurenti M. et al., 2022, A&A, 657, A57
Lightman A. P., White T. R., 1988, ApJ, 335, 57
Liu H. et al., 2019, ApJ, 878, 79
Liu H., Luo B., Brandt W. N., Brotherton M. S., Gallagher S. C., Ni Q., Shemmer O., Timlin J. D. I., 2021, ApJ, 910, 103
Liu T. et al., 2022, A&A, 661, A5
Lusso E. et al., 2012, MNRAS, 425, 623

Lusso E. et al., 2020, A&A, 642, A150
Marconi A., Axon D. J., Maiolino R., Nagao T., Pastorini G., Pietrini P., Robinson A., Torricelli G., 2008, ApJ, 678, 693
Marconi A., Axon D. J., Maiolino R., Nagao T., Pietrini P., Risaliti G., Robinson A., Torricelli G., 2009, ApJ, 698, L103
Marinucci A. et al., 2016, MNRAS, 456, L94
Marinucci A., Vietri G., Piconcelli E., Bianchi S., Guainazzi M., Lanzuisi G., Stern D., Vignali C., 2022, A&A, 666, A169
Matzeu G. A., Reeves J. N., Braito V., Nardini E., McLaughlin D. E., Lobban A. P., Tombesi F., Costa M. T., 2017, MNRAS, 472, L15
Middei R., Bianchi S., Marinucci A., Matt G., Petrucci P. O., Tamborra F., Tortosa A., 2019, A&A, 630, A131
Mosquera A. M., Kochanek C. S., Chen B., Dai X., Blackburne J. A., Chartas G., 2013, ApJ, 769, 53
Nardini E. et al., 2015, Science, 347, 860
Nardini E. et al., 2019, A&A, 632, A109
Nasa High Energy Astrophysics Science Archive Research Center (Heasarc), 2014, Astrophysics Source Code Library, record ascl:1408.004
Novikov I. D. , Thorne K. S. , 1973, in Dewitt C., Dewitt B. S., eds, Black Holes (Les Astres Occlus). p. 343
Onken C. A. et al., 2019, PASA, 36, e033
Onken C. A. et al., 2022, PASA, 39, e037
Panagiotou C., Papadakis I. E., Kammoun E. S., Dovčiak M., 2020, MNRAS, 499, 1998
Panagiotou C., Papadakis I., Kara E., Kammoun E., Dovčiak M., 2022, ApJ, 935, 93
Predehl P. et al., 2021, A&A, 647, A1
Reeves J. N., Braito V., Porquet D., Lobban A. P., Matzeu G. A., Nardini E., 2021, MNRAS, 500, 1974
Risaliti G., Elvis M., Fabbiano G., Baldi A., Zezas A., Salvati M., 2007, ApJ, 659, L111
Risaliti G., Young M., Elvis M., 2009, ApJ, 700, L6
Roming P. W. A. et al., 2005, Space Sci. Rev., 120, 95
Saxton R. D. et al., 2022, Astron. Comput., 38, 100531
Schlafly E. F., Finkbeiner D. P., 2011, ApJ, 737, 103
Scoville N., Norman C., 1995, ApJ, 451, 510
Shakura N. I., Sunyaev R. A., 1973, A&A, 24, 337
Shemmer O., Brandt W. N., Netzer H., Maiolino R., Kaspi S., 2008, ApJ, 682, 81
Shen Y., 2013, Bull. Astron. Soc. India, 41, 61
Simmonds C., Buchner J., Salvato M., Hsu L. T., Bauer F. E., 2018, A&A, 618, A66
Strüder L. et al., 2001, A&A, 365, L18
Tashiro M. et al., 2018, in den Herder J.-W. A. , Nikzad S. , Nakazawa K. eds, Proc. SPIE Conf. Ser. Vol. 10699, Space Telescopes and Instrumentation 2018: Ultraviolet to Gamma Ray. SPIE, Bellingham. p. 1069922,
Tortosa A. et al., 2023, MNRAS, 519, 6267
Turner M. J. L. et al., 2001, A&A, 365, L27
Ursini F., Dovčiak M., Zhang W., Matt G., Petrucci P. O., Done C., 2020, A&A, 644, A132
Vaughan S., Edelson R., Warwick R. S., Uttley P., 2003, MNRAS, 345, 1271
Virtanen P. et al., 2020, Nature Methods, 17, 261
Wilms J., Allen A., McCray R., 2000, ApJ, 542, 914
Wolf C. et al., 2018, PASA, 35, e010
Zappacosta L. et al., 2020, A&A, 635, L5

APPENDIX A: LINE SCAN

Despite the fact that an absorbed power law model explains the data well, some residuals in absorption (emission) could be seen at ∼1.3 keV (6.5 keV), rest frame, in the *XMM-Newton* spectra. We performed a scan of the *XMM-Newton* data in the full observed range

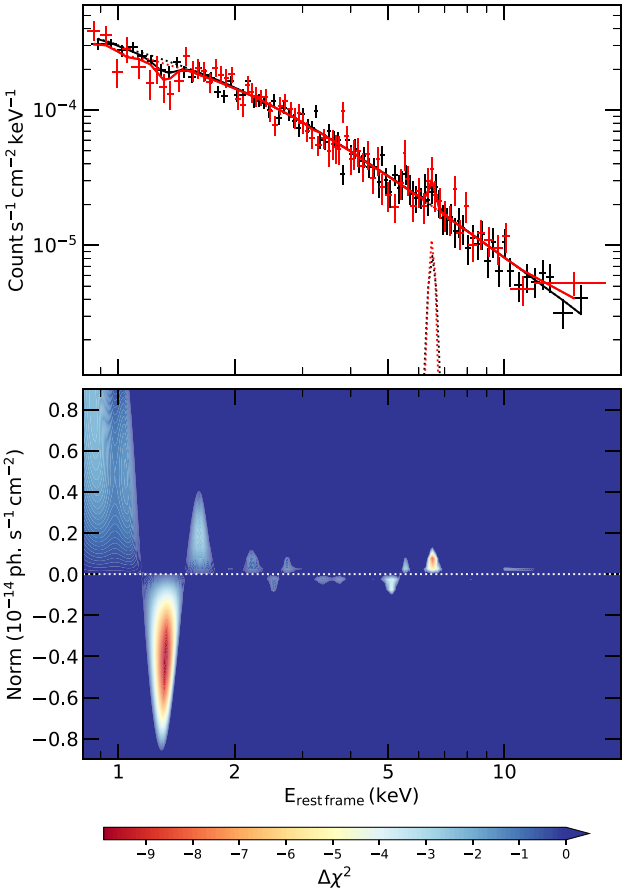

Figure A1. Top: XMM-Newton spectra (PN/MOS in black/red) fitted with a power law model, adding two Gaussian lines at 1.3 keV (in absorption) and 6.5 keV (in emsission), rest frame. Bottom: The improvement of the fit of the *XMM-Newton* spectra, obtained by adding an absorption/emission line to the model.

to check for the significance of the lines by adding a Gaussian line in emission or absorption with a fixed width $\sigma = 0.05$ keV. The results, presented in Fig. A1, show an improvement of the quality of the fit by $\Delta\chi^2 = -9.9$ and -8.9 (for two additional free parameters) by adding an absorption line at 1.32 keV and emission at 6.5 keV. Refitting the *XMM-Newton* spectra by adding these two lines and letting the width as a free parameter results in equivalent widths $EW_{\rm abs}(1.3\,{\rm keV}) = -25 \pm 10$ eV and $EW_{\rm em}(6.5\,{\rm keV}) = 117 \pm 44$ eV, with a total improvement of the fit by $\Delta\chi^2 = -19.5$ ($\sim 3\sigma$). The fit obtained by adding these features is shown in the upper panel of Fig. A1. It is worth noting that the origin of the absorption line may not be identified. However, the emission line at 6.5 keV could be associated with the Fe Kα emission line.

APPENDIX B: RESIDUALS

We show in this appendix the residuals obtained by modelling the X-ray spectra of J1144 from *Swift*, *XMM-Newton*, and *NuSTAR* observations as shown in Section 3.2.

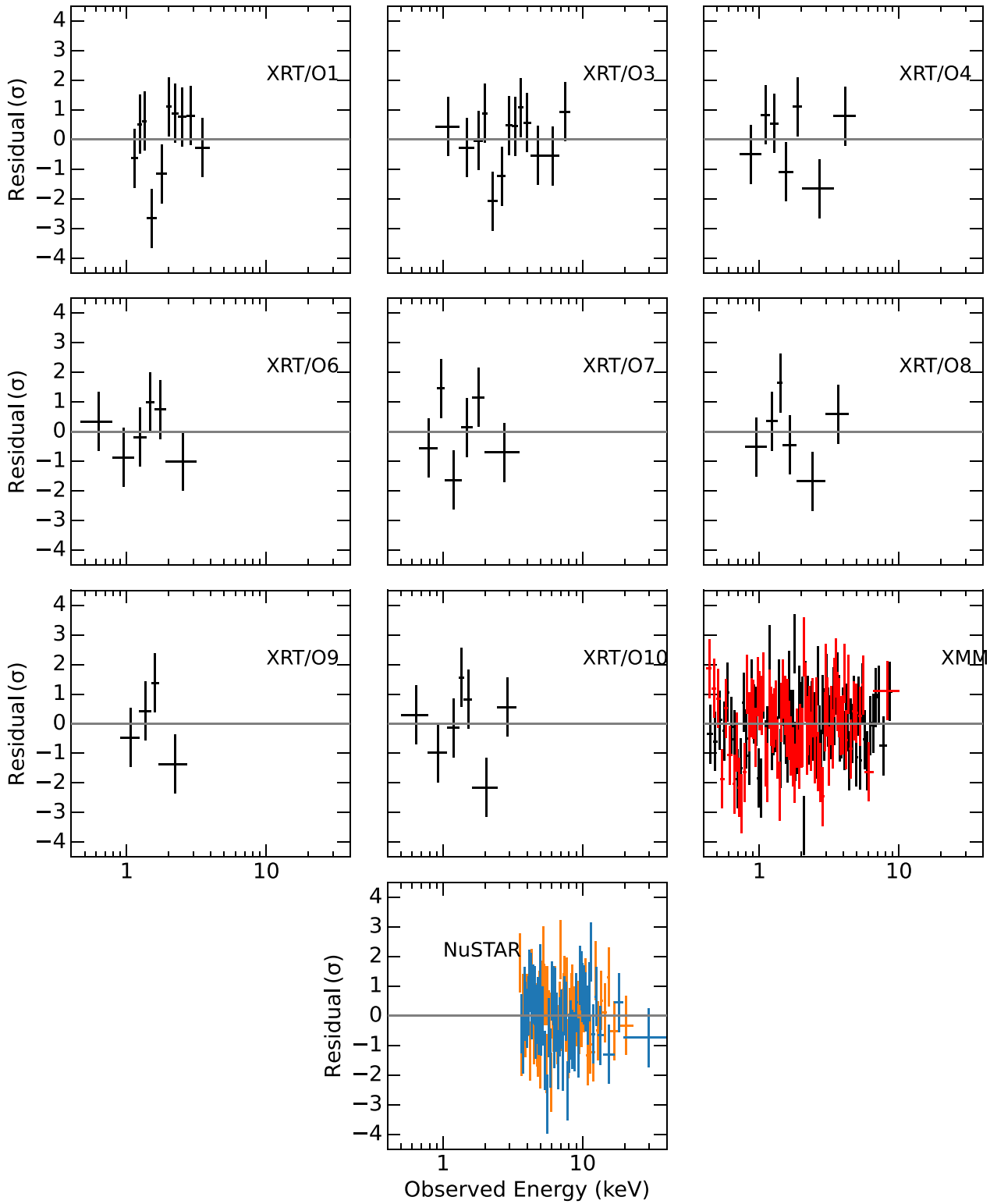

Figure B1. Residuals obtained by modelling the X-ray spectra of J1144 obtained from *Swift*, *XMM-Newton*, and *NuSTAR* observations using an aborbed power law with a high-energy cutoff (see Section 3.2).

APPENDIX C: CONTOURS

Fig. C1 shows the confidence contours obtained from fitting the eRASS spectrum as described in Section 2.1. Figs C2 and C3 show the confidence contours from modelling the SED of J1144 with `KYNSED` and `AGNSLIM`, respectively.

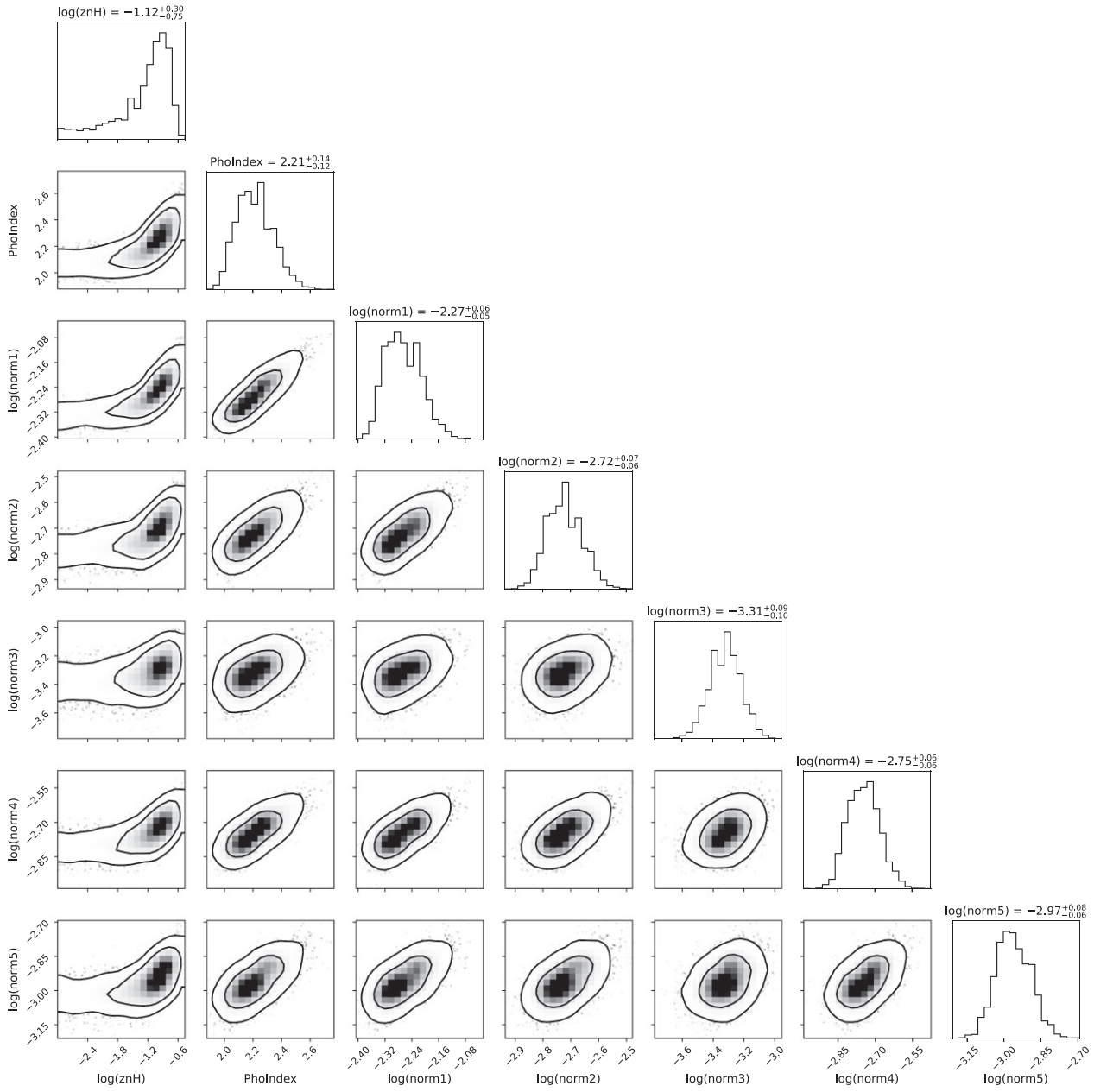

Figure C1. Corner plot showing the various parameters from fitting the eROSITA spectra.

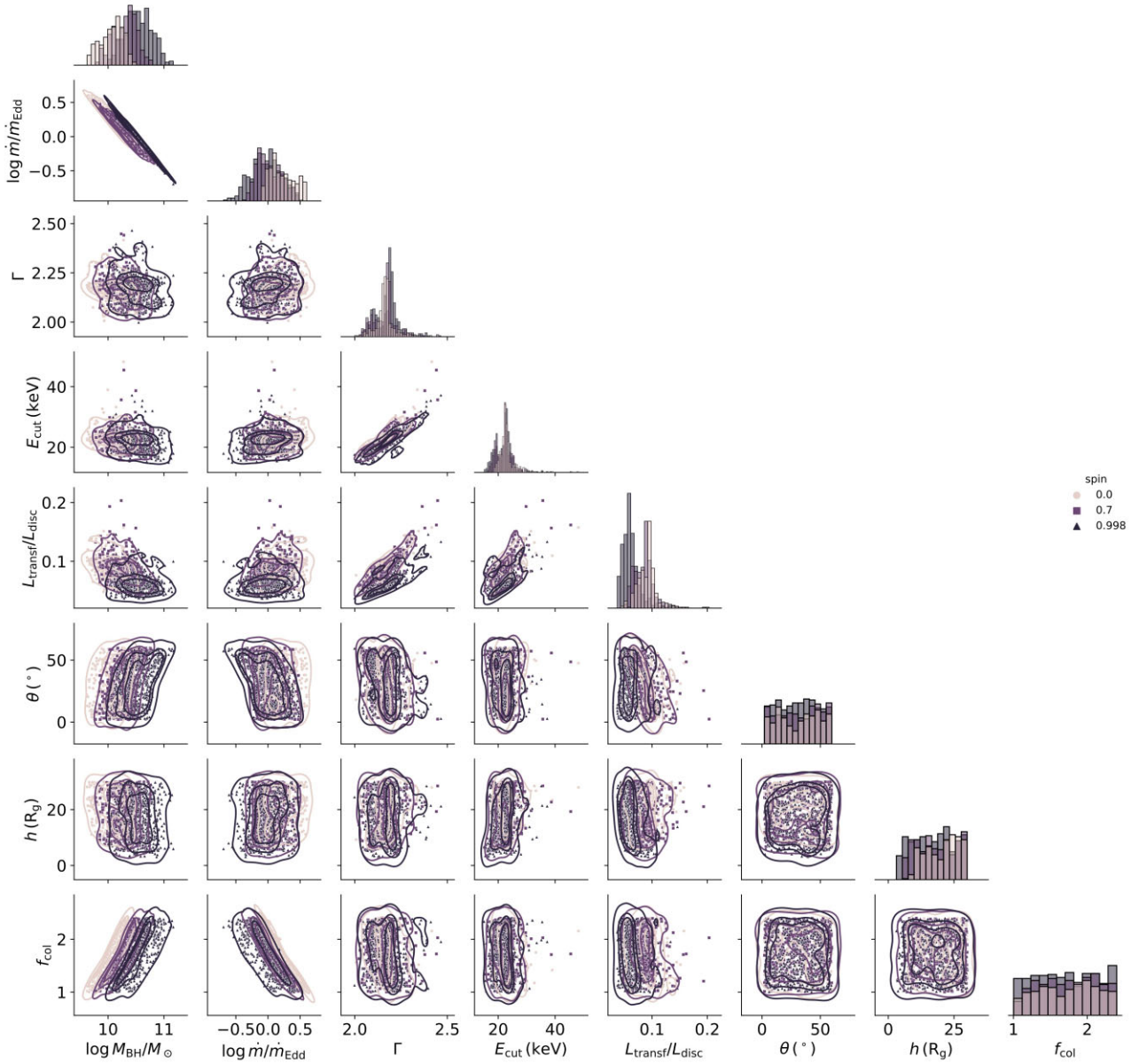

Figure C2. Corner plot showing the various parameters for modelling the SED using KYNSED. Circles, squares, and triangles correspond to spin values of 0, 0.7, and 0.998, respectively.

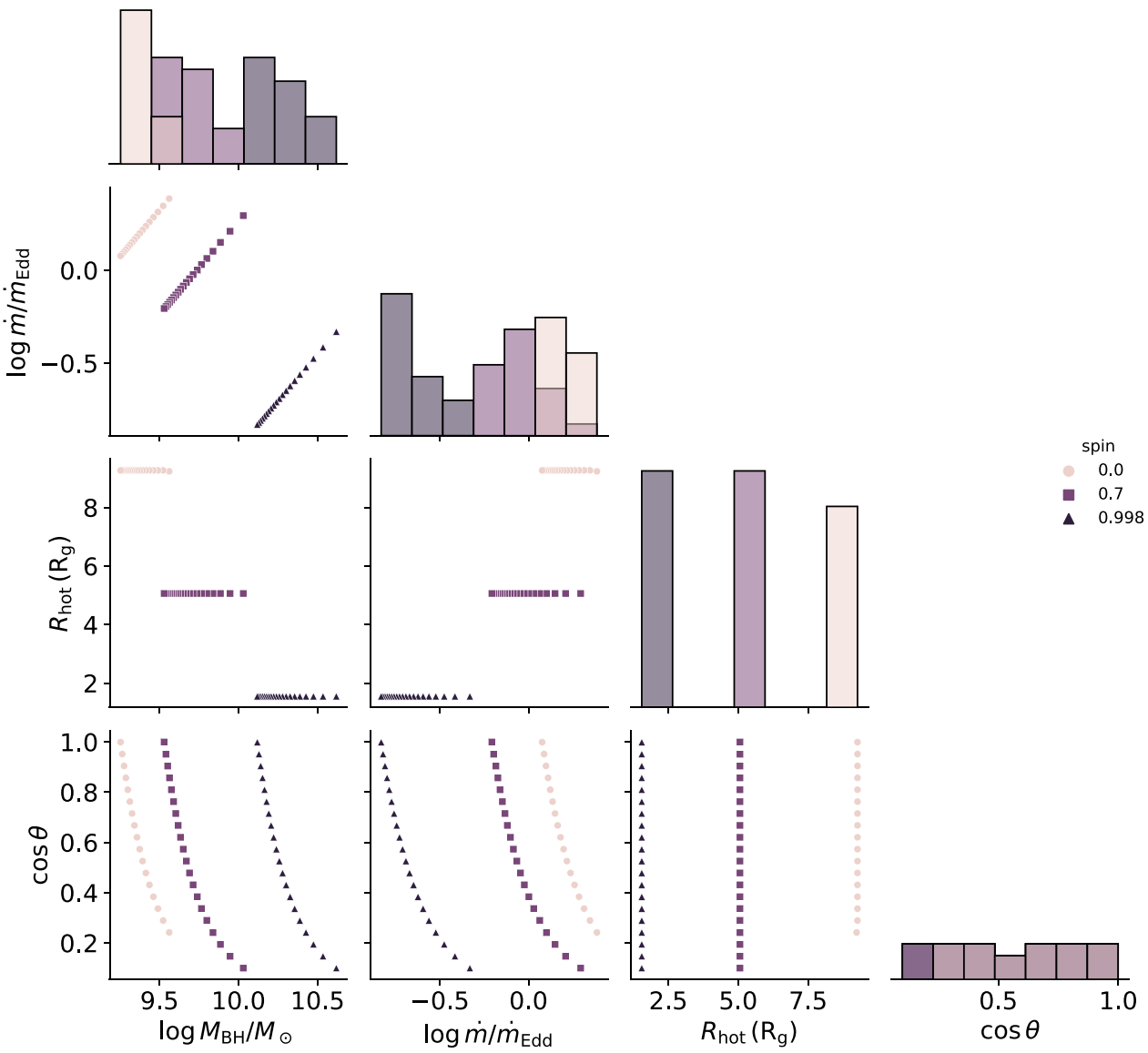

Figure C3. Corner plot showing the various parameters for modelling the SED using AGNSLIM. Circles, squares, and triangles correspond to spin values of 0, 0.7, and 0.998, respectively.

APPENDIX D: COMPARING KYNSED AND AGNSLIM

In this section, we investigate in further detais the differences between KYNSED and AGNSLIM in the sub-Eddington regime. In fact, as Kubota & Done (2019) mention, AGNSLIM should be consistent with a standard accretion rate a $\dot{m}/\dot{m}_{\rm Edd} \lesssim 2.39$. It is only above this limit that the local flux at the emissivity peak goes above the Eddington limit (see their fig. 1). We consider two values of the BH spin $a^* = 0$ and $a^* = 0.998$. We also considered $\dot{m}/\dot{m}_{\rm Edd} = 0.1$ and 1. For both models, we consider a mass of $10^{10}\,{\rm M}_\odot$, an inclination of 0°, and $\Gamma = 2$. For KYNSED we assume a coronal height of $10\,r_{\rm g}$, $E_{\rm cut} = 50$ keV, and $L_{\rm transf}/L_{\rm disc} = 0.1$. As for AGNSLIM, we assume $kT_{\rm h} = 25$ keV, and an $R_{\rm h}$ equivalent to the radius that contains 10 per cent of the disc power (as shown in fig. 1 of Dovčiak et al. 2022). This radius corresponds to $\sim 18\,r_{\rm g}$ and $1.8\,r_{\rm g}$, for $a^* = 0$ and 0.998, respectively. In order to fairly compare the two models we assumed a colour correction $f_{\rm col} = 1$ for KYNSED.

The resulting spectra are shown in Fig. D1. At low spin, the disc emission is slightly larger for AGNSLIM as compared to KYNSED. This difference increases as the spin increases. This discrepancy is most likely due to the fact that AGNSLIM does not take general relativity (GR) effects into account. Due to GR effects, a large amount of flux from the inner disc will end up in the BH and the disc, hence the difference in the two spectra. We note that Dovčiak et al. (2022) found the same difference between AGNSED (Kubota & Done 2018) and KYNSED at high spin values. However, they found a different behaviour for a non-spinning BH. This is mainly due to the fact that contrary to AGNSED, AGNSLIM assumes that for low accretion rates, the accretion disc extends down to the ISCO, giving a better agreement with KYNSED.

Similar to what Dovčiak et al. (2022) found, AGNSLIM overestimates the X-ray emission. In order to compensate for this,

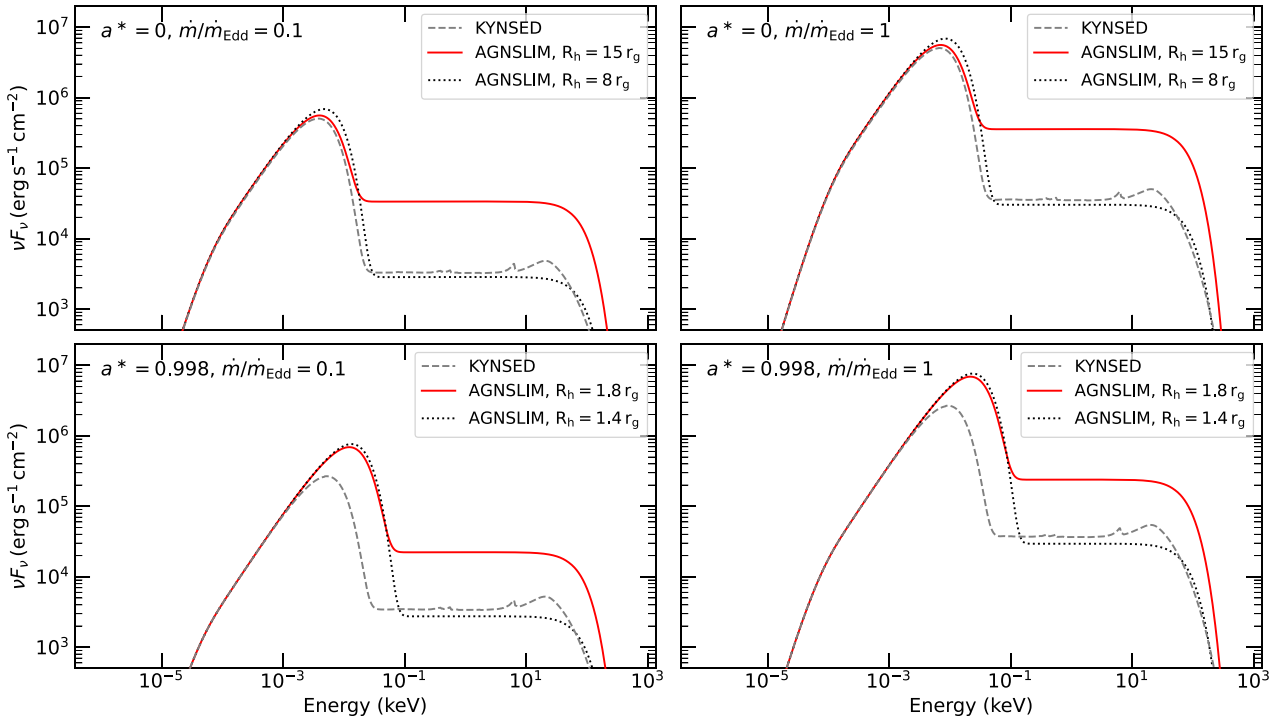

Figure D1. Comparison between KYNSED and AGNSLIM. The top (bottom) panels show the spectra for $a^* = 0$ (0.998). The right-hand and left-hand panels show the spectra for $\dot{m}/\dot{m}_{\rm Edd} = 0.1$ and 1, respectively. The grey dashed spectra correspond to KYNSED. The solid red spectra correspond to AGNSLIM assuming a hot X-ray corona size of $R_{\rm h} = 18\,r_{\rm g}$ and $1.8\,r_{\rm g}$ for $a^* = 0$ and 0.998, respectively. The black dotted lines show the same but assuming $R_{\rm h} = 8\,r_{\rm g}$ and $1.4\,r_{\rm g}$ for $a^* = 0$ and 0.998, respectively (See Section D for more details).

we decreased the size of the X-ray region in AGNSLIM to $8\,r_{\rm g}$ and $1.4\,r_{\rm g}$ for $a^* = 0$ and 0.998, respectively. This brings the X-rays in the two models to the same level, but slightly increases the difference in the UV/optical. As discussed in section 3.3 in Dovčiak et al. (2022), this difference arises from two factors: (a) in KYNSED, the disc flux is emitted as the cosine of the inclination while the X-rays are isotropic, and (b) despite the fact that a fraction $L_{\rm transf}/L_{\rm disc}$ is assumed in KYNSED to be transferred to the corona, a smaller fraction in fact reaches the observer at infinity. This translates into a smaller X-ray source size in AGNSLIM.

This paper has been typeset from a TEX/LATEX file prepared by the author.